

REPORT DOCUMENTATION PAGE				Form Approved OMB No. 0704-0188	
<p>Public reporting burden for this collection of information is estimated to average 1 hour per response, including the time for reviewing instructions, searching existing data sources, gathering and maintaining the data needed, and completing and reviewing the collection of information. Send comments regarding this burden estimate or any other aspect of this collection of information, including suggestions for reducing the burden, to Department of Defense, Washington Headquarters Services, Directorate for Information Operations and Reports (0704-0188), 1215 Jefferson Davis Highway, Suite 1204, Arlington, VA 22202-4302. Respondents should be aware that notwithstanding any other provision of law, no person shall be subject to any penalty for failing to comply with a collection of information if it does not display a currently valid OMB control number.</p> <p>PLEASE DO NOT RETURN YOUR FORM TO THE ABOVE ADDRESS.</p>					
1. REPORT DATE (DD-MM-YYYY) 28-01-2010		2. REPORT TYPE Final Report		3. DATES COVERED (From – To) 15 October 2008 - 28-Jan-10	
4. TITLE AND SUBTITLE Investigation of a Nanowire Electronic Nose by Computer Simulation			5a. CONTRACT NUMBER FA8655-08-1-3082		
			5b. GRANT NUMBER		
			5c. PROGRAM ELEMENT NUMBER		
6. AUTHOR(S) Dr. Andrew P Horsfield			5d. PROJECT NUMBER		
			5d. TASK NUMBER		
			5e. WORK UNIT NUMBER		
7. PERFORMING ORGANIZATION NAME(S) AND ADDRESS(ES) Imperial College London South Kensington Campus London SW7 2AZ United Kingdom			8. PERFORMING ORGANIZATION REPORT NUMBER N/A		
9. SPONSORING/MONITORING AGENCY NAME(S) AND ADDRESS(ES) EOARD Unit 4515 BOX 14 APO AE 09421			10. SPONSOR/MONITOR'S ACRONYM(S)		
			11. SPONSOR/MONITOR'S REPORT NUMBER(S) Grant 08-3082		
12. DISTRIBUTION/AVAILABILITY STATEMENT Approved for public release; distribution is unlimited.					
13. SUPPLEMENTARY NOTES					
14. ABSTRACT <p>Checking planes for explosives, monitoring food quality and testing human breath for signs of disease are some of the applications of electronic noses. The ideal electronic nose would respond to a large number of chemicals over a range of concentrations. Many devices have been proposed and built which can be optimised to detect particular sets of compounds, but generally lack the ability to be tuned to detect user specified molecules while in operation. Typical devices use metal oxides, conducting polymers, piezoelectric crystal or fibre optics. Many of the mechanisms depend on rather specific chemical properties of the odorant (such as being oxidising or reducing agents), or are difficult to modify to accommodate new chemical species. This is in striking contrast to the human nose which can respond to endless new chemical species provided only that the molecules are small enough to fit the receptors. We are developing a versatile electronic nose that can be tuned to respond to a particular type of molecule simply by the application of a bias. The design is motivated by a recent theory of odorant detection in humans that was in turn inspired by Inelastic Electron Tunnelling Spectroscopy (IETS). The theory proposes that molecular recognition occurs when the exchange of energy between a molecular vibration and a mobile electron enables the electron to move from one site to another. Electronic noses are of interest to the defense of civilian flights as they can be used to detect explosives in the hold of passenger aircraft. More generally they can be used to detect the presence of molecules that could be a threat to human health. With the design proposed here, quite general scans of molecules are possible simply by sweeping the set of biases applied to an array of detectors. In this project we will investigate the properties of one freestanding nanowire TBDW RTD by means of computer simulation with a view to proposing a design suitable for subsequent fabrication and then characterization.</p>					
15. SUBJECT TERMS EOARD, Sensor Technology, electronic nose, molecule detection					
16. SECURITY CLASSIFICATION OF:			17. LIMITATION OF ABSTRACT UL	18. NUMBER OF PAGES 44	19a. NAME OF RESPONSIBLE PERSON WYNN SANDERS, Maj, USAF
a. REPORT UNCLAS	b. ABSTRACT UNCLAS	c. THIS PAGE UNCLAS			19b. TELEPHONE NUMBER (Include area code) +44 (0)1895 616 007

Investigation of a Nanowire Electronic Nose by Computer Simulation

Andrew Horsfield and Lianheng Tong

April 14, 2009

Department of Materials, Imperial College London, South Kensington Campus, London SW7 2AZ, U.K.

Report to the European Office of Aerospace Research and Development

Award Number FA8655-08-1-3082

Contents

1	Summary	6
2	Introduction	7
3	Methods, Assumptions and Procedures	10
3.1	Experimental Setup	10
3.2	Effective mass approximation calculations	12
3.2.1	The Potential Profile	12
3.2.2	The Electron Current	15
3.2.3	Localized states in wells	18
3.3	Density Functional Theory Calculations	19
3.3.1	InAs and InP Structures Used For DFT Calculation	20
3.3.2	The Choice of Exchange-Correlation Functional	21
3.3.3	Spin-Orbit Contributions	22
3.3.4	The Choice of Basis Set	23
4	Results and Discussions	25
4.1	Density Functional Theory Calculations	25
4.1.1	InAs and InP Bulk	25
4.1.2	InAs-InP Nanowires	25
4.2	Effective mass approximation calculations	33
4.2.1	Single barrier devices	33
4.2.2	Double barrier devices	33
4.2.3	Triple barrier devices	35
5	Conclusions	39
6	List of Symbols, Abbreviations and Acronyms	43

List of Figures

1	Left: cartoon of original IETS experimental setup. Right: cartoon of the Turin mechanism of odorant identification.	8
2	Cartoon of the potential profile for the nanowire resonant tunneling device under bias. The shaded areas are populated by electrons.	9
3	a) Device with a single InP barrier. b) Device with two InP barriers that create an InAs quantum dot.	10
4	The left panel shows electrical characteristics for the single barrier device, while the right panel shows the characteristics for a double barrier device.	11
5	Left: The band offset at InAs-InP junction. Right: Variation of current with temperature, with effective barrier heights indicated; taken from [3].	12
6	The single barrier device under an applied bias.	13
7	Regions in the one barrier device with different chemical potential.	14
8	Plot of $\Delta v(z)$	15
9	The nanowire is treated as a perfect cylinder with infinitely hard walls.	15
10	We divide the device into several regions, each with distinct potential and effective mass. . .	17
11	Potential profile of a single well	19
12	Zinc-blend structure.	21
13	The unit cells we used in our DFT calculation. Each of the sub-cells of InAs (or InP) contains 4 atoms – 2 In and 2 As (or P). The periodic condition is demonstrated by the 8 atoms unit cell.	22
14	InAs bulk band structure calculated using LDA. Note that there is no band gap at the Fermi energy.	23
15	Band structure of bulk InAs along the line Γ to X . Note that the primitive unit cell is used. .	25
16	Total and projected densities of states for bulk InAs.	26
17	Band structure of bulk InP along the line Γ to X . Note that the primitive unit cell is used. .	26
18	Total and projected densities of states for bulk InP.	27
19	Band structures of InAs-InP nanowire having repeating units of 1 InAs unit cell and 1 InP unit cell (8 atoms unit cell), 2 InAs and 2 InP (16 atoms) and 8 InAs and 8 InP (64 atoms) respectively.	28
20	The projected densities of states from the 64 atoms unit cell calculation for the InAs unit cells at the middle of InAs region and at the interface of the nanowire device.	29
21	The projected densities of states from the 64 atoms unit cell calculation for the InP unit cells at the middle of InP region and at the interface of the nanowire device.	29
22	The total density of states from the 64 atoms unit cell calculation.	30
23	Band structure of the 128 atoms unit cell InAs-InP nanowire.	31
24	The projected densities of states from the 128 atoms unit cell calculation for the InAs unit cells at the middle of InP region and at the interface of the nanowire device.	31
25	The projected densities of states from the 128 atoms unit cell calculation for the InP unit cells at the middle of InAs region and at the interface of the nanowire device.	32
26	The total density of states from the 128 atoms unit cell calculation.	32
27	Current versus voltage for two single barrier devices at room temperature. The blue curve corresponds to a barrier width of 70Å, and the red curve to a barrier width of 800Å. A carrier concentration of 10^{-7-3} was assumed, and temperature is 300K.	33
28	Current versus voltage for a double barrier device at 4.2K for two carrier concentrations. The red curve corresponds to a carrier concentration of 10^{-8-3} and the blue curve to $5 \times 10^{-9-3}$	34
29	This figure shows the transmission probability as a function of energy for a range of bias voltages. A delta function approximation to the transmission is good, with the peak transmission being strongly dependent on voltage.	34
30	This figure shows how the transmission varies as the wire radius is increased from 200Å (left) to 300Å (right).	35

31	These figures show the effect of varying the <i>outer</i> barriers. Plotted is the variation of electron transmission with respect to the energy of the incident electron with no bias applied. The well width is 150\AA and the middle barrier width is 20\AA in both cases. In the left panel the outer barrier width is 10\AA while in the right panel it is 20\AA	36
32	These figures show the effect of varying the <i>middle</i> barrier width. Plotted is the variation of electron transmission with respect to the energy of the incident electron with no bias applied. The well width is 150\AA and the outer barrier width is 20\AA in both cases. In the left panel the middle barrier width is 10\AA while in the right panel it is 20\AA	36
33	These figures show the variation of electron transmission with respect to the energy of the incident electron with no bias applied. All the barrier widths are 30\AA in both cases. In the left panel the well width is 150\AA while in the right panel it is 100\AA . Note that the maximum transmission in each channel should be 1. The apparent drop in maximum transmission below 1 in the left panel is a result of a lack of resolution of the plots.	37
34	These figures show the transmission as a function of the electron energy, and refer to a nanowire with outer barrier widths of 20\AA , center barrier width of 25\AA , and well widths of 100\AA . In the left panel the bias is zero, while in the right panel the bias is 0.1V	38
35	These figures shows the variation of electric current with bias. The left panel has results at two temperatures (4K and 300K), and refers to a nanowire with outer barrier widths of 20\AA , center barrier width of 25\AA , and well widths of 100\AA . The right panel has results for 300K with wider barriers (all 30\AA).	38
36	This figure displays the current as a function of voltage for two values of the carrier density in the leads. There is roughly factor of 10 increase in the current for a factor of 10 increase in the carrier density. All calculations are at 300K with well widths of 100\AA , outer barrier widths of 20\AA , and middle barrier width of 25\AA	39
37	A cartoon indicating the use of a gate to increase the density of carriers in the active region.	40

List of Tables

1	These vibrational frequencies are taken from the “Tables of Molecular Vibrational Frequencies Consolidated Volume I” produced by Shimanouchi [30].	9
2	Table of values of x_{ml} which that $J_m(x_{ml}) = 0$, for $m = 1, 2, 3$	16
3	Tables of minimum energies of individual channels for two wire radii. Left table, $R=200\text{\AA}$; right table $R=250\text{\AA}$	17
4	Energies of lowest levels in a single well.	19
5	The basis sets for CRYSTAL available to us for our calculations.	24
6	Comparison between different basis sets. ΔE is the change in total energy with basis set relative to that for the pVDZ-PP basis set.	24
7	Variation of electron chemical potential with dopant density at room temperature.	37

1 Summary

In this report we propose a novel design for a chemical sensor which, if successful, would provide a new paradigm for chemical sensors. It operates by systematically probing a universal physical property (atomic vibrations), and would be tuneable simply by the application of a bias voltage. This is in contrast to typical sensors currently available (including those based on nanowires) which are finely tuned to specific chemical species, and often exploit charge transfer reactions. We suggest that the new sensors be made from InAs with InP layers, as there is a high level of existing expertise available for constructing nanowires from them. The InP will be used to form three barriers between which will lie two quantum wells. This design could pave the way for versatile sensors compatible with standard semiconductor devices that could be compact, low power, fast and selective.

The operation of these devices is inspired by a proposed mechanism for odorant recognition in human beings suggested by Luca Turin, and becoming increasingly plausible as new experiments are performed to test it. The devices operate as follows. The quantum wells formed in the InAs wires by the InP barriers contain localized and sharp electronic states that define reference energies. When a bias is applied along the length of the wire the levels in one well become offset relative to those in the other. Under these conditions the elastic resonant tunneling possible with zero bias is frustrated. However, if an electron traveling from a state in one well to a state in the neighboring one can exchange the right amount of energy with a neighboring odorant molecule by making it oscillate, then resonance can be restored. The resulting rise in current is the signal that a molecule with the right vibrational frequency is present, and we have a device acting as a sensor.

Here we report the calculations we have performed to characterize this novel nanowire device. Two types of calculation are considered. For the first, we use a simple scheme (effective mass approximation) to produce a device simulator that predicts the variation of current with applied bias (the basic electrical characteristics of the device). This simulator was written specifically for this project, and gives us control over the approximations used, and was tailored for the needs of this work. The second type of calculation is based on a first principles method (density functional theory), and gives atomic level information. It turned out that the choice of approximation that we make is very important (hybrid functionals are essential for providing a correct description of the electrons). These precise calculations cannot be used yet to give the current as a function of bias (we do not have access to suitable software), but they give information that can be related directly to the electrical properties. They therefore act as an important check on the results from our device simulator. For the 50Å and 150Å wells we see clear signatures of the localized states in the InAs wells in the band structure and the densities of states. Furthermore we can see the tapering out of the resonances at the interface between the wells and the barriers.

Using our device simulator we have investigated the dependence of the design parameters (the widths of the tunneling barriers, the widths of the quantum wells, the radius of the nanowire, the density of dopants and the temperature). We find that the two outer InP barriers control the width of the resonances in the quantum wells. This contributes to the resolution of the device (how far apart two vibrational frequencies must be to be distinguished), and the total electric current. The middle barrier determines the interaction between the resonances in the wells, and needs to be thick enough to prevent too strong a coupling, but not so wide as to reduce the current below measurable levels. The widths of the quantum wells must be large enough to allow charge injection into the lowest resonant state, but small enough to keep the resonances far enough apart so that odorants do not excite electrons inside a well (reducing the selectivity of the device).

Using the data acquired, we have identified a promising candidate device. It has a radius of 200Å, has two outer barriers of width 30Å between which is a third barrier also of width 30Å. The distance between the outer barriers and the middle barrier (the quantum well width) is 100Å. We believe this device should have the necessary properties at room temperature, though a gate may need to be added to control the carrier concentration.

2 Introduction

Checking planes for explosives and nerve agents, monitoring food quality and testing human breath for signs of disease are some of the applications of chemical sensors. The ideal sensor would respond to a large number of chemicals over a range of concentrations in a way that is easy to interpret. Many devices have been proposed and built which can be optimized to detect particular sets of compounds, but generally lack the ability to be tuned to detect user specified molecules while in operation. A few of the more important devices are as follows [7, 9, 16]:

- Metal-oxide semiconductors can change their electrical resistance when chemical species adsorb onto their surfaces. Oxygen in the atmosphere oxidizes the surface (removes electrons from the conduction band) lowering the conductivity. Reducing gases adsorbed onto the surface can increase the conductivity by injecting electrons into the conduction band. The main problems with this method are the need to run at high temperature, the limited selectivity, and the susceptibility to poisoning of the surface. Metal oxides can also be used in Field Effect Transistors (FET) in which the exposed gates are made from catalysts whose charge varies when gases are adsorbed, thereby modifying the channel conductance.
- Conducting polymers vary their conductance when molecules are adsorbed, so molecules can be detected by the change in current. The polymers can be tuned for specific systems by modifying attached groups or counter-ions. The main problems with this approach are the very long response times, inherent time- and temperature-dependent drift, poor batch-to-batch reproducibility and the high cost of sensor fabrication. A variation on this involves putting conducting carbon-black powder into a polymer which is then painted across the foils of a capacitor. Diffusion of gas phase molecules into the polymer creates a characteristic swelling which separates the conducting particles and increasing the measured resistance across the capacitor. Polymers have also recently been used for chemical FETs.
- Piezoelectric crystals change their vibrational frequencies when molecules bind to the surface. Selectivity can be achieved by the use of surface coatings. The main problems with this method are batch-to-batch reproducibility and the difficulty of replacing sensors. A variation of this is to use atomic force microscope cantilevers, and monitor their change in resonance frequency when molecules adsorb.
- Fiber-optic chemical sensors use a dye whose fluorescence emission spectrum is very sensitive to the polarity of its surroundings, and which is embedded in a polymer matrix. By varying the polymer, different responses can be achieved. The polymers swell when molecules diffuse in, which can be detected from the change in fluorescence, and hence monitored optically. While they are fast, small, versatile and inexpensive, their lifetimes are limited by photobleaching and they require additional sophisticated instruments for monitoring.
- Ion mobility spectrometry involves the separation of species after ionization by means of an electric field. Species separate according to their mobilities.
- Infrared spectroscopy has a long and highly successful history of identifying molecules, and is now used as part of chemical sensors. It works by probing the vibrational frequencies of molecules by using light with the same frequency as the vibrations. Particularly important for sensors is nondispersive infrared (NDIR) in which the absorption of a single frequency of light is monitored. A clear limitation is the fact that the frequency is fixed rather than tuneable, and thus restricted to detecting those molecules that have vibrational modes with that frequency. This is the device most close to the one we propose here.

More recently there has been huge interest in the use of carbon nanotubes as chemical sensors. There is an excellent recent review by Kauffman and Star[18] of the current state of the art. Clearly great sensitivity can be achieved because of the delicate nature of the electronic structure of carbon nanotubes which is

easily disrupted by adsorbates, leading to an easily measurable change in conductivity. However, traditional mechanisms (notably charge transfer) with their inherent limitations are being applied (such as having to design specific sensors for particular gases).

It is clear from the above that there are many ingenious suggestions for electronic noses, and that they have a certain degree of flexibility, but there are hard constraints nevertheless. Many of the mechanisms depend on rather specific chemical properties (such as being oxidizing or reducing agents), or are difficult to modify to accommodate new chemical species. This is in contrast to the human nose that can respond to endless new chemical species, provided the molecules are small enough to fit the receptors.

We plan to develop a versatile chemical sensor that can be tuned to respond to a particular type of molecule simply by the application of a bias. The design is motivated by a recent theory of odorant detection in humans[6, 35] that was in turn inspired by Inelastic Electron Tunneling Spectroscopy (IETS)[1]. The theory proposes that molecular recognition occurs when the exchange of energy between a molecular vibration and a mobile electron enables the electron to move from one site to another. IETS has a long history of being used to identify organic molecules[22, 32]. Recently it has been considered by the group of David Galipeau as a means to construct a chemical sensor employing the original device structure (two metal films separated by an insulating layer), but has not been completely successful[5].

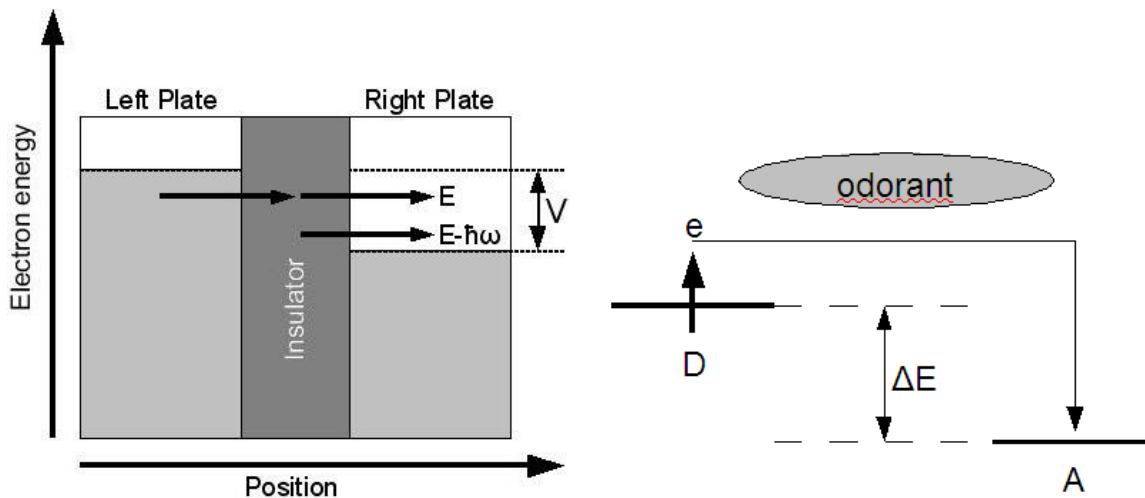


Figure 1: Left: cartoon of original IETS experimental setup. Right: cartoon of the Turin mechanism of odorant identification.

To understand why that implementation has been problematic consider the original IETS experimental setup (see figure 1). The current is measured as a function of bias V , where the electrode plates are conventional metals and the insulating layer contains the sample whose vibrational structure is to be probed. When $V > \hbar\nu$ (where ν is the vibrational frequency of the oscillators coupling to the tunneling electrons and \hbar is Planck's constant) it becomes possible for electrons to excite phonons and tunnel to the right hand side. Elevated temperatures produce broadening of the Fermi surfaces of the metals (which introduces uncertainty in the voltage at which inelastic tunneling begins) and allow thermally excited oscillators to give up energy to the electrons (which introduces additional contributions to the current). Both of these factors degrade the resolution of the spectrometer as temperature increases, thus forcing the measurements to be made at low temperature.

On the other hand the proposed biological mechanism (which must operate at body temperature) is based on two narrow reference electronic levels thereby overcoming this difficulty[6, 35, 36] (see the right-hand side of Figure 1). The electron starts in the donor level (labelled D in Figure 1) and has an energy corresponding to that level that is insensitive to temperature. It can tunnel to the acceptor level (labelled A in Figure 1) which also has a well defined energy that is ΔE less than the donor energy. However, to conserve energy the

Molecule	Group	Mode	Energy (cm-1)	Energy (eV)
Benzene	C-H	stretch	3062	0.38
		bend	1326-673	0.16-0.08
	Ring	deform	1010-410	0.13-0.05
Methanol	O-H	stretch	3681	0.46
	C-O	stretch	1033	0.13
Acetic acid	C=O	stretch	1788	0.22
	C=O	bend	642	0.08

Table 1: These vibrational frequencies are taken from the “Tables of Molecular Vibrational Frequencies Consolidated Volume I” produced by Shimanouchi [30].

mobile electron must lose ΔE in energy to something else. The energy could be lost by exciting a neighboring odorant molecule provided it can vibrate with a frequency ν such that $\Delta E = h\nu$. In the Turin theory of odorant identification, the successful arrival of an electron at the acceptor site indicates the presence of an odorant.

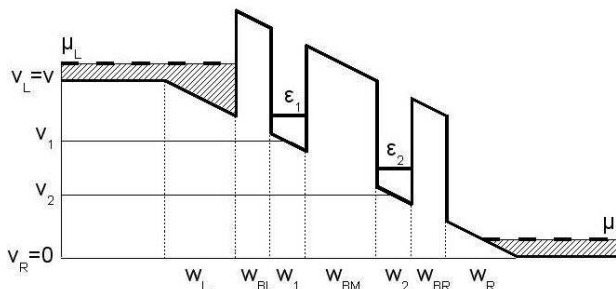


Figure 2: Cartoon of the potential profile for the nanowire resonant tunneling device under bias. The shaded areas are populated by electrons.

We anticipate using a semiconductor nanowire containing a triple barrier, double well resonant tunneling diode (TBDW RTD) to provide similar sharp levels in a solid-state device. We assume the device will be made from InAs with InP for the potential barriers: this choice of materials is made because of the huge experience now gained using them to construct very thin wires with atomically sharp interfaces (see, for example, [4, 8, 10]). The chemical selectivity of the device is tuned by adjusting the energy splitting between these levels by applying a voltage (see Figure 2). This selectivity is the key property of the device that distinguishes it from currently existing chemical sensors.

Typical vibrational frequencies of common molecular groups are well known. Some examples are shown in Table 1. The main conclusion to draw from this table is that typical frequencies are of order 0.1eV, and we would like a resolution of about 0.01eV to be able to distinguish between groups.

Below we describe calculations to determine the characteristics of nanowire devices. What we want to know is the variation of the current with applied bias (the I-V curve). We have constructed a simple device simulator to compute this. It also provides the probability of transmission of an electron of a given energy through the device: this information makes interpretation of the I-V characteristics much easier. This simulator is based on a very simple model of electron motion (the effective mass approximation) and so is unable to provide certain information. Thus we have also carried out density functional theory (DFT) calculations that give us more detailed information about the electronic structure. In particular it provides insight into what happens at the interface between the InAs and InP regions (atomic rearrangement, charge transfer, electron energy gap, etc.).

However, we stress that we can only make promising *suggestions* for devices here because there are necessary approximation we must make. Features we know to be missing include: the distribution of dopant atoms,

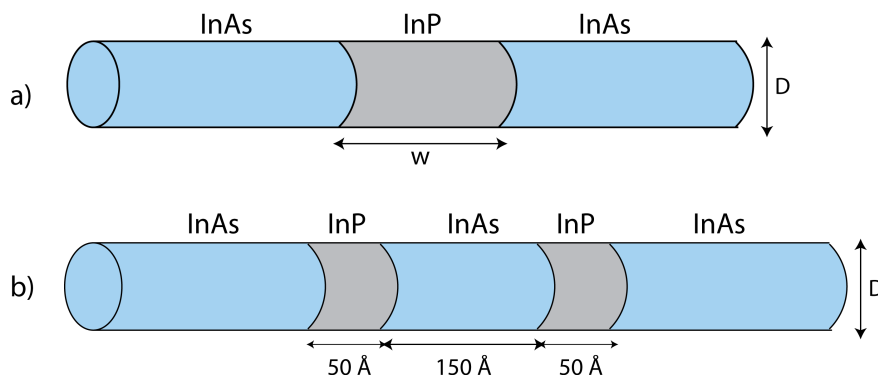


Figure 3: a) Device with a single InP barrier. b) Device with two InP barriers that create an InAs quantum dot.

the effect of the environment (which will be able to exchange energy with the current carrying electrons), electron-phonon interactions in the device, electron repulsion within the quantum wells (possibly leading to Coulomb blockade at low temperatures) and electron-electron scattering. To obtain a full understanding the devices will need to be investigated experimentally.

3 Methods, Assumptions and Procedures

3.1 Experimental Setup

As discussed above, the devices we are interested in are nanowires made from InAs with regions of InP introduced to act as barriers to electron flow. These devices are connected at each end to a DC power source, and the precise dependence of the current that flows on the applied voltage will be determined by the thickness of the wire, the width, number and spacing of the InP barrier, the temperature, and the number of free carriers in the leads. Our purpose here is to determine by computer modeling this variation of current with voltage.

An important experimental demonstration of the properties of these devices has been reported in two seminal papers by Björk in 2002 [3, 4]. Two devices are considered in the latter paper, one with a single InP barrier, and one with two barriers that create an InAs quantum dot (see Figure 3). The nanowire heterostructures are fabricated by the vapor-liquid-solid technique using gold nano-particle as the metal catalyst. The In, P and As are introduced as molecular species in which one atom of In, P or As is bound to hydrocarbons. These hydrocarbons introduce a small amount of carbon impurities ($10^{-16}/\text{cm}^3$), which in turn act as electron donors, and hence define the number of free carriers available.

The electrical characteristics for the single barrier device are shown in Figure 4. We see that making the barrier thicker reduces the current. For the thick barrier the current is due to thermionic excitations as there is very little tunneling. This allows the effective barrier height due to InP to be found. It depends on the applied voltage because charge accumulation modifies the potential the electrons see, but for zero bias it is found to be about 0.6V^1 . Using the known band gaps[19] for InAs (0.43 eV) and InP (1.42 eV) we obtain the band offset diagram given in the left panel of Figure 5. With two barriers, we obtain a resonance in the current at about 80 mV bias at 4.2 K. This is attributed to a narrow quantized state in the quantum dot. This feature is important for this project as the electronic chemical sensor is designed to operate by the inelastic transfer of charge between two such states in neighboring quantum wells. This feature is analyzed below.

An important characteristic experimental quantity is the size of the electric currents. These are of order $10^{-12}\text{A} \rightarrow 10^{-9}\text{A}$ [3]. These correspond to 10^7 to 10^{10} e/s. For the largest current this corresponds to

¹This is obtained from the equation $I(V, t) = \text{const} T^2 e^{eV/kT}$, and the data is shown in the right panel of Figure 5

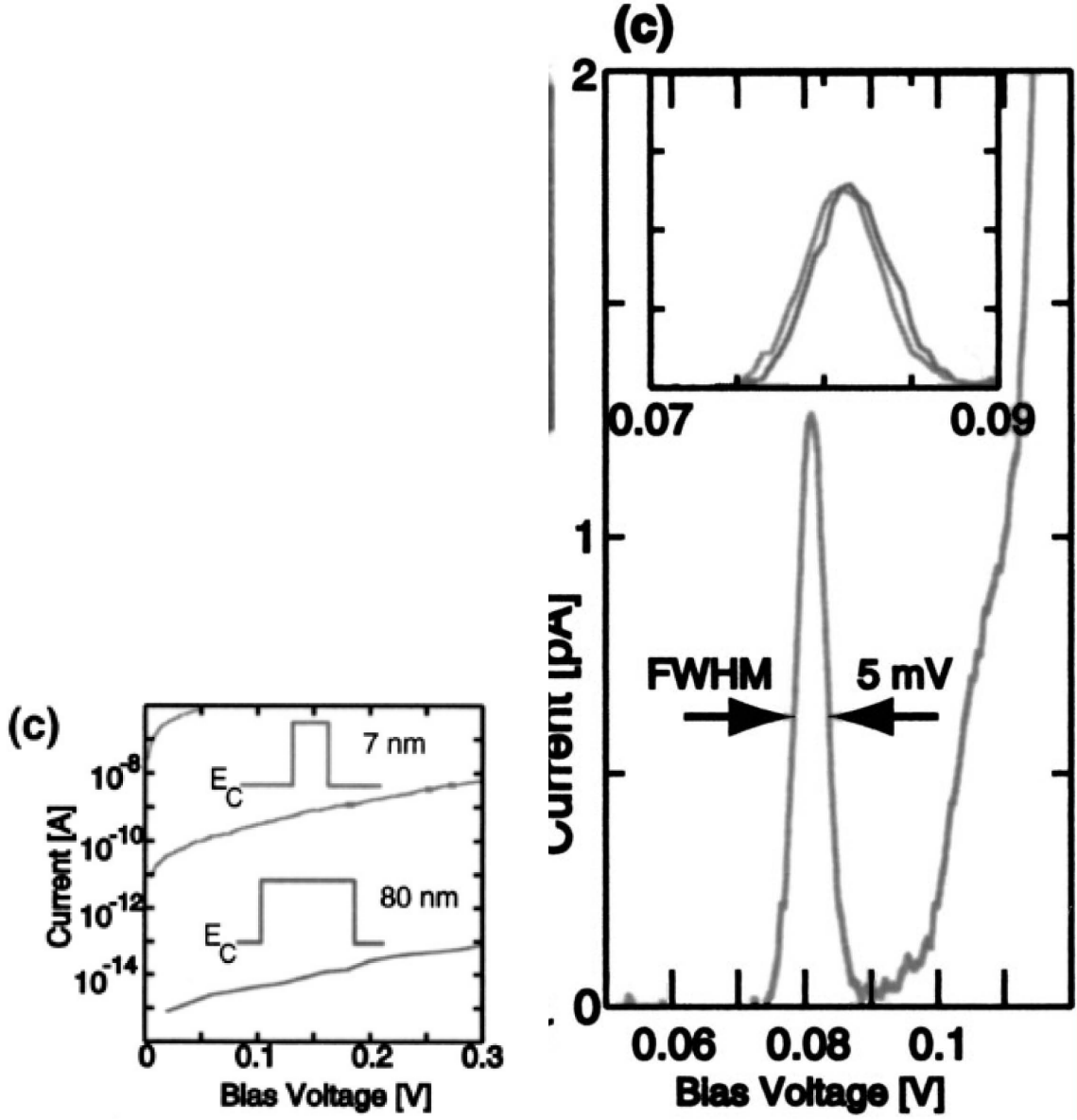


Figure 4: The left panel shows electrical characteristics for the single barrier device, while the right panel shows the characteristics for a double barrier device.

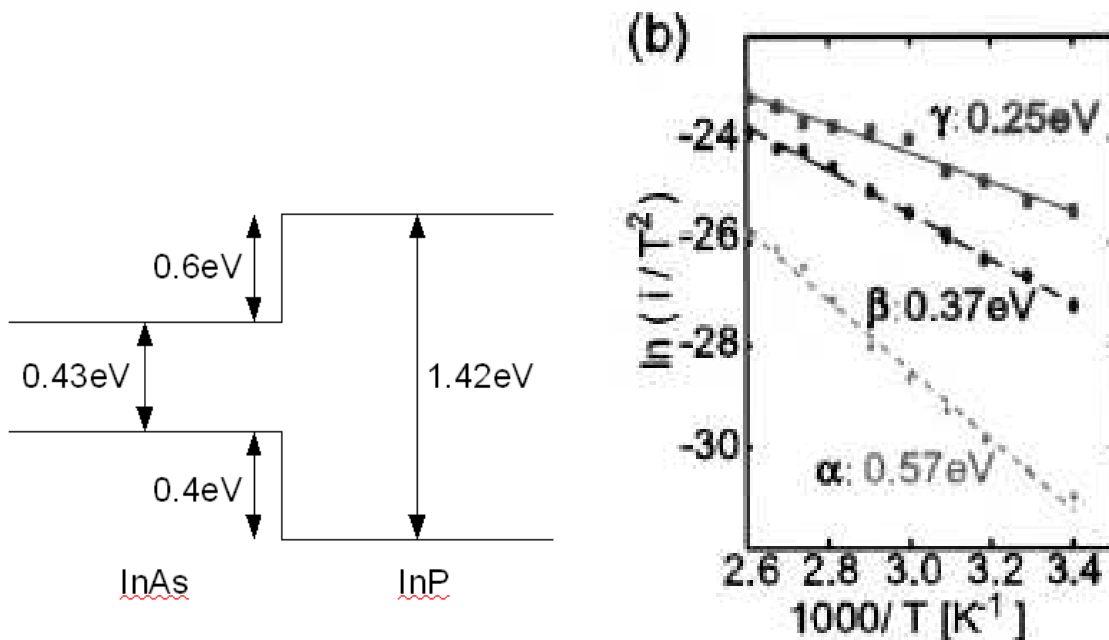


Figure 5: Left: The band offset at InAs-InP junction. Right: Variation of current with temperature, with effective barrier heights indicated; taken from [3].

one electron running through the device every 10^{-10} s. Using the expression for the mobility $e\tau/m^*$ and noting that for InAs its value is about $30,000\text{cm}^2\text{V}^{-1}\text{s}^{-1}$ [19], we can estimate the time between collisions (τ) which is of order 10^{-13} s. Thus an electron will make of order 10^3 collisions between successive escapes past the barriers. We can therefore conclude that the electrons will be in equilibrium in the leads. This is an important fact we will exploit in our calculations.

3.2 Effective mass approximation calculations

The theory of electron motion used for the device simulator is the effective mass approximation, a technique frequently used to determine the properties of nanoscale electronic devices. It starts from the electron wavefunctions and energies obtained from band theory, and then uses a set of approximations to provide an efficient way to compute the effect of small changes in the potential. The resulting equation look like the Shrödinger equation, except that the potential is now the perturbation, the wave function is a smooth envelope function, and all the complexity of the crystal is taken account of through a change in the electron mass. For more information see Chapter 4 of “Theory of Defects in Solids” by Stoneham [33]. Below we summarize some of the technical points implemented in our device simulator to perform self-consistent calculations of electric current flow within this approximation.

3.2.1 The Potential Profile

The manner in which electrons travel through the nanowire depends sensitively on the potential landscape. We have noted the strong effects of the InP barriers. But when a bias is applied, charge will accumulate within the wire, and this will generate electric fields that will also modify the potential landscape. We now discuss the set of approximations we have used to estimate this potential profile.

Because the electrons in the nanowire leads (the regions either side of the central region containing the InP barrier) are at equilibrium, they can be characterized by chemical potentials μ_L and μ_R for the left and right leads respectively (see figure 6). In general, the electron chemical potential is the energy gained (lost) when

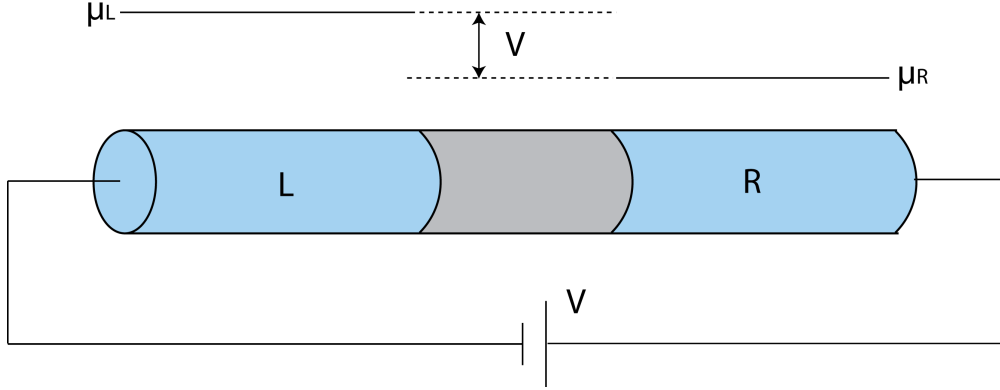


Figure 6: The single barrier device under an applied bias.

an electron is added (removed) from system. In Figure 6 the battery provides the energy ($\Delta\mu = \mu_L - \mu_R$) needed to transfer an electron from the right lead to the left. The maximum energy the battery can provide to an electron is eV (where V is the voltage of the battery), thus electron transfer stops when $\Delta\mu = eV$ (equilibrium). From this argument we see that the difference in chemical potential originates with an excess of electrons in the left lead and a corresponding deficit in the right lead. The electrons will then arrange themselves so as to minimize their energy. We thus have the outlines of a practical scheme for finding the potential profile: we have two regions with different chemical potentials that will reach equilibrium when the electrons relax to minimize their energies, subject to the chemical potential difference being kept fixed at the bias potential from the battery.

To fill in the computational details, consider the Kohn-Sham formalism of Density Functional Theory (DFT)[26]. This gives us a recipe for finding a potential for the electrons from the density,

$$v(\mathbf{r}) = v_{\text{ext}}(\mathbf{r}) + \int d^3\mathbf{r}' \frac{\rho(\mathbf{r}')}{4\pi\epsilon_0|\mathbf{r} - \mathbf{r}'|} + v_{\text{xc}}[\rho] \quad (1)$$

for finding the density from the wavefunctions of the electrons,

$$\rho(\mathbf{r}) = \sum_n f_n |\psi_n(\mathbf{r})|^2 \quad (2)$$

and for finding the wavefunctions from the potential

$$\frac{-\hbar^2}{2m} \nabla^2 \psi_n + v \psi_n = \epsilon_n \psi_n \quad (3)$$

This procedure is computationally expensive, so we use an approximation based on the assumption that the *change* in potential in a given lead due to the application of a bias is *slowly* varying. If the density is $\rho_0(\mathbf{r}, \bar{\mu} - \bar{v})$ for a given chemical potential $\bar{\mu}$ in the isolated lead with average potential \bar{v} , and the change in potential is $\Delta v(\mathbf{r})$, then the approximation we shall use is that $\rho(\mathbf{r}) \approx \rho_0(\mathbf{r}, \mu - \bar{v} - \Delta v(\mathbf{r}))$. This is good provided electrons remain coherent only over distances that are small relative to distances over which the potential varies.

If the change in potential is dominated by classical electrostatics (which is certainly the case for the interaction *between* the leads, but less obviously so within a given lead) then we can make the Hartree approximation, in which case the change in potential satisfies the Poisson equation:

$$\nabla^2 \Delta v(\mathbf{r}) = - \left[\frac{\rho(\mathbf{r}) - \rho_0(\mathbf{r})}{\epsilon_0 \epsilon_r} \right] e^2 \quad (4)$$

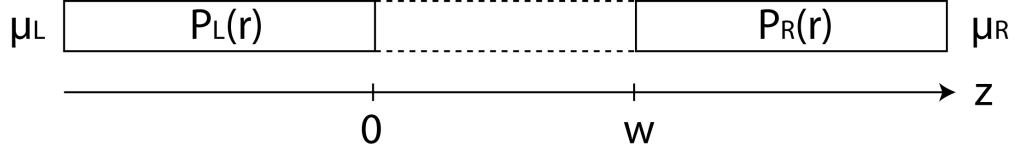


Figure 7: Regions in the one barrier device with different chemical potential.

Let the nanowire be aligned along the z axis (see Figure 7). The important variations in the potential are thus also along the z axis, so we shall neglect the variations in x and y for a given z . Thus we have:

$$\begin{aligned} \frac{d^2 \Delta v}{dz^2} &\approx -\frac{e^2}{\epsilon_0 \epsilon_r} (\rho(z) - \rho_0(z)) \\ &\approx -\frac{e^2}{\epsilon_0 \epsilon_r} [\rho_0(z, \mu(z) - \bar{v} - \Delta v(z)) - \rho_0(z, \bar{\mu} - \bar{v})] \end{aligned} \quad (5)$$

where $\mu(z) = \mu_L$ in the left lead, $\mu(z) = \mu_R$ in the right lead, and $\rho(z) - \rho_0(z) = 0$ between the leads (i.e. $\mu(z) - \Delta v(z) = \bar{\mu}$). We can solve equation (5) for the device region immediately (see figure 7):

$$\Delta v(z) = \Delta v(0) + e\mathcal{E} \cdot z \quad 0 \leq z \leq w \quad (6)$$

To estimate the potential in the leads we make a linear approximation:

$$\rho_0(z, \mu(z) - \bar{v} - \Delta v(z)) - \rho_0(z, \bar{\mu} - \bar{v}) \approx \begin{cases} -\Delta v(z) \frac{\partial \rho_0}{\partial \mu}(z, \bar{\mu} - \bar{v}) & z < 0 \\ -(\Delta \mu + \Delta v(z)) \frac{\partial \rho_0}{\partial \mu}(z, \bar{\mu} - \bar{v}) & z > w \end{cases} \quad (7)$$

where we have set $\mu_L = \bar{\mu}$. We now make our final approximation, which is to treat $\partial \rho_0 / \partial \mu$ as a constant². We now define $\gamma^2 = (e^2 / \epsilon_0 \epsilon_r) \partial \rho_0 / \partial \mu$, and Poisson's equation now becomes:

$$\frac{d^2 \Delta v}{dz^2} = \begin{cases} +\gamma^2 \Delta v & z < 0 \\ 0 & 0 \leq z \leq w \\ +\gamma^2 (\Delta \mu + \Delta v) & z > w \end{cases} \quad (8)$$

The boundary conditions are $\Delta v(-\infty) = 0$ and $\Delta v(+\infty) = -\Delta \mu$. This has the solution:

$$\Delta v(z) = \begin{cases} -\frac{\Delta \mu}{2+\gamma w} e^{\gamma z} & z \leq 0 \\ -\frac{\Delta \mu}{2+\gamma w} (1 + \gamma z) & 0 \leq z \leq w \\ \Delta \mu + \frac{\Delta \mu}{2+\gamma w} e^{\gamma(w-z)} & z \geq w \end{cases} \quad (9)$$

When the device simulator includes band bending in the leads, the linear response solution above is used as an initial guess, and is then refined by an explicit solution of Poisson's equation. This is achieved by writing equation (5) as a finite difference equation:

$$\frac{1}{\delta^2} [v_{n+1} - 2v_n + v_{n-1}] = -\frac{e^2}{\epsilon_0 \epsilon_r} \Delta \rho_n \quad (n \in \{0, \dots, N-1\}) \quad (10)$$

where δ is the spacing between neighboring mesh points, which is then solved using a very efficient algorithm from Numerical Recipes (**tridag**) subject to the boundary conditions $v_{-1} = 0$ and $v_N = -\Delta \mu$.

The distance over which the potential varies in the leads is governed by the quantity α . This depends strongly on the number of free carriers. For the concentration found from the dopants experimentally

²This can be justified on the basis that the smooth envelope functions of the effective mass approximation average over the atomic detail.

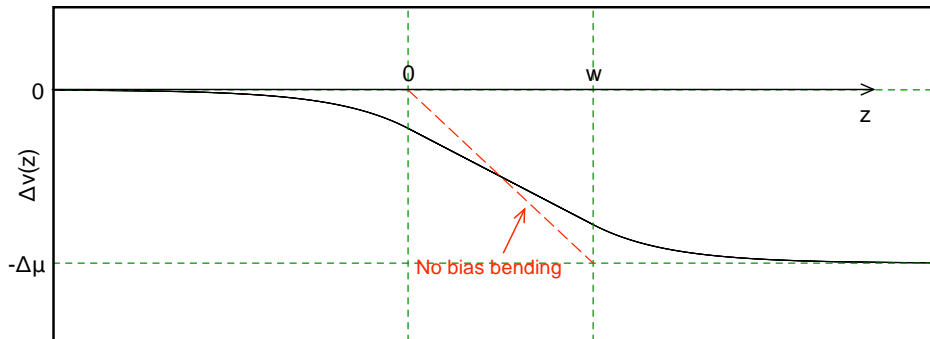
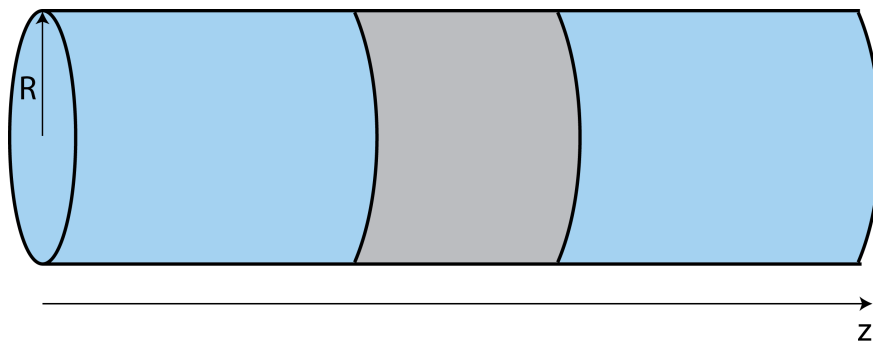

 Figure 8: Plot of $\Delta v(z)$.


Figure 9: The nanowire is treated as a perfect cylinder with infinitely hard walls.

($\sim 10^{16} \text{cm}^{-3}$ [37]), $\alpha \sim 6 \times 10^{-3} \text{\AA}^{-1}$, which gives a distance of $1/\gamma \sim 170 \text{\AA}$. This is quite a large distance, so band bending in the leads can probably be neglected in the transport calculations. Furthermore, it is unclear whether including band bending always improves the accuracy. The problem is the following. The formalism for computing the current assumes that the electrons arrive from $\pm\infty$ and undergo no scattering until they reach the device ($0 \leq z \leq w$). This means that the electrons in the well (energies < 0) to the left of the device ($z < 0$) formed by the charge redistribution do not contribute. But this contradicts our earlier discussion about the electrons being in thermal equilibrium: this requires substantial scattering in the leads resulting in all states having a thermal population. Once thermal equilibrium is reached, all the electrons can contribute to the current. Thus it might be better to ignore band bending, but adjust the bias to include the effect of the potential drop in the leads. From our simple linear response calculation the voltage drop is $2\Delta\mu/(2 + \gamma w) = \Delta\mu/(1 + \gamma w/2)$, which could be a significant fraction of the applied voltage. Using values for the RTD of Björk, $w = 250 \text{\AA}$, and $\gamma \sim 6 \times 10^{-3} \text{\AA}^{-1}$ giving the drop as $0.57\Delta\mu$.

In the simulations below we have decided to ignore band bending in the leads, and have just retained the linear voltage drop across the device.

3.2.2 The Electron Current

To compute the electron current we need wavefunctions, which means we need to solve Schrödinger's equation. Here we describe the formalism for a simple scheme within the effective mass approximation, from which we obtain expressions that we can easily compute and interpret.

We treat the nanowire as a perfect cylinder with infinitely hard walls (figure 9). Further, we assume that the potential is piecewise constant down the length of the tube, depending only on z , and not r or θ . In one

l	J_0	J_1	J_2
1	2.4048	3.8317	5.1356
2	5.5201	7.0156	8.4172
3	8.6537	10.1735	11.6198

 Table 2: Table of values of x_{ml} which that $J_m(x_{ml}) = 0$, for $m = 1, 2, 3$.

of these regions Schrödinger's equation is

$$-\frac{\hbar^2}{2m^*}\nabla^2\psi + V\psi = E\psi \quad (11)$$

where the electron is assigned an effective mass m^* which depends on the region. The boundary condition on the wavefunction is that ψ goes to zero at $r = R$. Writing the Laplacian in cylindrical polar coordinates we get:

$$\nabla^2\psi = \frac{\partial^2\psi}{\partial r^2} + \frac{1}{r}\frac{\partial\psi}{\partial r} + \frac{1}{r^2}\frac{\partial^2\psi}{\partial\phi^2} + \frac{\partial^2\psi}{\partial z^2} \quad (12)$$

To allow us to separate variables we write the wavefunctions as

$$\psi(r, \phi, z) = R(r)\Phi(\phi)Z(z) \quad (13)$$

and Schrödinger's equation becomes:

$$\frac{R''}{R} + \frac{R'}{rR} + \frac{1}{r^2}\left(\frac{\Phi''}{\Phi}\right) + \left(\frac{Z''}{Z}\right) = -\frac{2m^*}{\hbar^2}(E - V) = -\alpha^2 \quad (14)$$

To ensure that the left hand side is a constant we require Φ''/Φ and Z''/Z to be constant. This gives:

$$\left. \begin{aligned} \Phi(\phi) &= e^{im\phi} \\ Z(z) &= e^{iqz} \end{aligned} \right\} \quad (15)$$

where m is an integer to ensure $\Phi(\phi + 2\pi m) = \Phi(\phi)$. The radial equations is then:

$$\frac{R''}{R} + \frac{R'}{rR} - \frac{m^2}{r^2} = (q^2 - \alpha^2) = -k^2 \quad (16)$$

which has the solutions $R(r) = J_{|m|}(kr)$ where $J_m(x)$ is a Bessel function of the first kind. The allowed values of k are determined by the boundary condition $J_{|m|}(kR) = 0$. Some values of x such that $J_{|m|}(x) = 0$ are given in table 2.

The total energy is thus given by:

$$E_{mlq} = V + \frac{\hbar^2}{2m^*}\left(q^2 + \frac{x_{|m|l}^2}{R^2}\right) \quad (17)$$

The energy thus is composed of three parts: the potential energy (V), a discrete set of contributions to the kinetic energy from angular and radial motion ($E_{ml}^\perp = (\hbar^2/2m^*)x_{|m|l}^2/R^2$) and a continuous contribution to the kinetic energy from the motion along the wire ($E_q^\parallel = \hbar^2 q^2/(2m^*)$). It is conventional to call a set of states characterized by given values of m and l a channel. Some values of E_{ml}^\perp for two wire radii are shown in Table 3.

To build up a wavefunction throughout the wire from the contributions in each region of constant potential we match wavefunctions at the interfaces. Consider two neighboring regions n and $n + 1$. Let z_n be the position of the left hand end of region n . (see figure 10). The wavefunction needs to be continuous everywhere,

l	J_0	J_1	J_2	l	J_0	J_1	J_2
1	0.024	0.061	0.109	1	0.015	0.039	0.070
2	0.126	0.204	0.293	2	0.081	0.130	0.188
3	0.310	0.429	0.559	3	0.198	0.274	0.358

Table 3: Tables of minimum energies of individual channels for two wire radii. Left table, $R=200\text{\AA}$; right table $R=250\text{\AA}$.

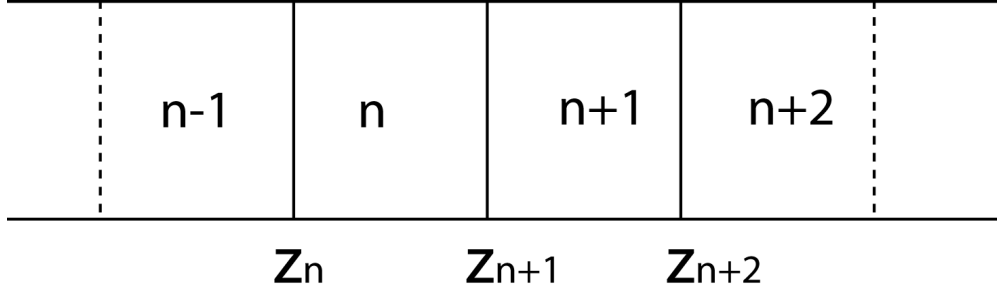


Figure 10: We divide the device into several regions, each with distinct potential and effective mass.

so $\psi_n(z_{n+1}) = \psi_{n+1}(z_{n+1})$. We cannot just match derivatives of the wavefunctions, as the effective mass in each region can be different. Thus we impose continuity of current, which gives:

$$\frac{1}{m_n^*} \frac{\partial \psi_n}{\partial z}(z_{n+1}) = \frac{1}{m_{n+1}^*} \frac{\partial \psi_{n+1}}{\partial z}(z_{n+1}) \quad (18)$$

For the wavefunctions to be continuous for every value of r and θ for a given z , m , l and $k = x_{|m|l}/R$ must be the same in every region. Thus the wavefunction in region n has the form

$$\psi_n(r, \phi, z) = e^{im\phi} J_{|m|}(kr) \left[A_n e^{iq_n(z-z_n)} + B_n e^{-iq_n(z-z_n)} \right] \quad (19)$$

with

$$q_n = \sqrt{\frac{2m_n^*}{\hbar^2} (E - V_n) - k_{|m|l}^2} \quad (20)$$

We thus must use the matching conditions to find the unknown coefficients A_n and B_n . This gives the following relationships between coefficients in neighboring regions:

$$\begin{pmatrix} A_n \\ B_n \end{pmatrix} = \begin{pmatrix} e^{-iq_n(z_{n+1}-z_n)} & 0 \\ 0 & e^{iq_n(z_{n+1}-z_n)} \end{pmatrix} \begin{pmatrix} \frac{1}{2} \left(1 + \frac{q_{n+1}}{q_n} \frac{m_n^*}{m_{n+1}^*} \right) & \frac{1}{2} \left(1 - \frac{q_{n+1}}{q_n} \frac{m_n^*}{m_{n+1}^*} \right) \\ \frac{1}{2} \left(1 - \frac{q_{n+1}}{q_n} \frac{m_n^*}{m_{n+1}^*} \right) & \frac{1}{2} \left(1 + \frac{q_{n+1}}{q_n} \frac{m_n^*}{m_{n+1}^*} \right) \end{pmatrix} \times \begin{pmatrix} A_{n+1} \\ B_{n+1} \end{pmatrix} \quad (21)$$

$$= \mathbf{P}_n \mathbf{M}_n \begin{pmatrix} A_{n+1} \\ B_{n+1} \end{pmatrix} \quad (22)$$

If we have N regions (labeled 1 to N), then we have:

$$\begin{pmatrix} \tilde{A}_1 \\ \tilde{B}_1 \end{pmatrix} = \begin{pmatrix} A_1 e^{iq_1(z_2-z_1)} \\ B_1 e^{-iq_1(z_2-z_1)} \end{pmatrix} = \mathbf{M}_1 \mathbf{P}_2 \mathbf{M}_2 \dots \mathbf{P}_{N-1} \mathbf{M}_{N-1} \begin{pmatrix} A_N \\ B_N \end{pmatrix} \\ = \mathbf{S} \begin{pmatrix} A_N \\ B_N \end{pmatrix} = \begin{pmatrix} S_{11} & S_{12} \\ S_{21} & S_{22} \end{pmatrix} \begin{pmatrix} A_N \\ B_N \end{pmatrix} \quad (23)$$

We have introduced \tilde{A}_1 and \tilde{B}_1 to avoid working with $z_1 = -\infty$. For a wave traveling in from the left and exiting on the right we can put $\tilde{A}_1 = 1$, $\tilde{B}_1 = R$; $A_N = t_N$ and $B_N = 0$. Then we have $t_N = 1/S_{11}$. The quantity $T = |t_N|^2$ is called the transmission, and as shown below is central to the computation of the electric current, and will be considered extensively in our analysis of devices. S_{11} is straightforward to compute by repeated multiplication of matrices, the number of multiplications depending on the number of slices into which the device is divided.

The choice of the number of regions depends on the shape of the potential profile. We are making the approximation that in one region the potential is a constant. For slowly varying potential this will be quite a good approximation for larger distances, whereas for rapidly varying potentials this will only be a good approximation over short distance. We have found that a spacing of 10Å is usually sufficient, though 1Å can be used if higher accuracy is needed.

To compute the electric current from left to right we use the expectation value of the current operator at $z = z_0$:

$$\hat{J}(z_0) = \frac{1}{2m^*}(\delta(z - z_0)\hat{p} + \hat{p}\delta(z - z_0)) \quad (24)$$

where \hat{p} is the momentum operator ($\hat{p} = -i\hbar\partial/\partial z$). If we evaluate the current to the right of the central region, then we know that the wavefunction has the form:

$$\psi_{mlq} = AJ_{|m|}(k_{ml}r)e^{im\phi}t_N e^{iq(z-z_N)} \quad (25)$$

where A is a normalization constant. The total current originating from the left is given by:

$$I_L = \sum_{mlq} 2 \int d^3\mathbf{r} \psi_{mlq}^* \hat{J}(z_0) \psi_{mlq} f(E_{mlq} - \mu_L) \quad (26)$$

where $f(\epsilon)$ is the Fermi function. This can be evaluated to give:

$$I_L = \sum_{ml} \frac{-e}{\pi\hbar} \int_{-\infty}^{+\infty} d\epsilon |t_N(\epsilon)|^2 f(\epsilon - \mu_L) \sqrt{\frac{\epsilon - \epsilon_{ml}^\perp - V_R}{\epsilon - \epsilon_{ml}^\perp}} \quad (27)$$

where V_R is the potential in the far right lead. If we include the contribution from the right hand side as well we get the total current:

$$I = \sum_{ml} \frac{-e}{\pi\hbar} \int_{-\infty}^{+\infty} d\epsilon |t_N(\epsilon)|^2 \sqrt{\frac{\epsilon - \epsilon_{ml}^\perp - V_R}{\epsilon - \epsilon_{ml}^\perp}} [f(\epsilon - \mu_L) - f(\epsilon - \mu_R)] \quad (28)$$

3.2.3 Localized states in wells

A key concept with the multiple barrier structures is that of resonant states localized in the wells between the barriers. To obtain an estimate of the energies of these levels we consider an isolated well (see Figure 11) with depth $V=0.6\text{eV}$. The effective electron mass in the well is taken to be that for InAs ($m_W^* = 0.023m_e$) and that for the surrounding region to be that for InP ($m_B^* = 0.08m_e$). The energies of the bound states can be found as solutions to the following two equations (one for even parity wavefunctions, and one for odd parity wavefunctions - *c.f.* Baym[2]),

$$\begin{aligned} \sqrt{\alpha - \beta x^2} + \beta x \cot(x/2) &= 0 & \text{odd wavefunctions} \\ \sqrt{\alpha - \beta x^2} - \beta x \tan(x/2) &= 0 & \text{even wavefunctions} \end{aligned} \quad (29)$$

where

$$\begin{aligned} \alpha &= \frac{m_B^*}{m_e} \left(\frac{a}{a_0}\right)^2 \frac{V}{Ry} \approx 0.012598 \left(\frac{a}{\text{\AA}}\right)^2 \\ \beta &= \frac{m_B^*}{m_W^*} \approx 3.48 \end{aligned} \quad (30)$$

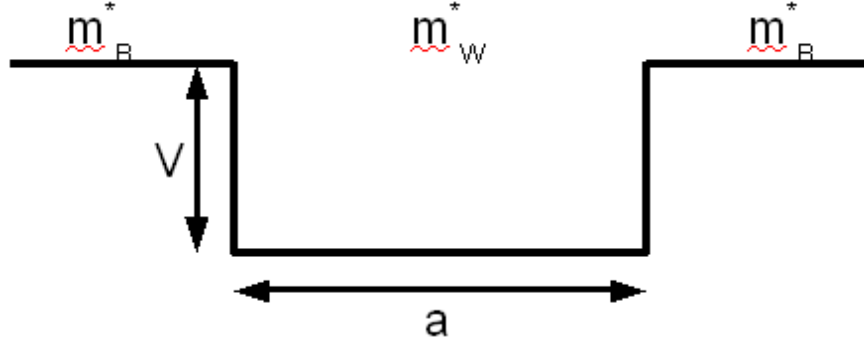


Figure 11: Potential profile of a single well

Well width (Å)	Energy (eV)
50	0.149
100	0.065
150	0.037
200	0.024

Table 4: Energies of lowest levels in a single well.

and the electron energy is given by

$$E = \frac{m_e}{m_W^*} \left(\frac{a_0}{a} \right)^2 x^2 Ry \approx 165.65 \left(\frac{\text{\AA}}{a} \right)^2 x^2 \text{ eV} \quad (31)$$

The energies of the lowest levels for several well widths are shown in Table 4. The lowest energy resonances below can be determined approximately by adding the numbers in this table to the lowest energies for the channels given in Table 3.

3.3 Density Functional Theory Calculations

To understand the electronic structure of the proposed InAs-InP nanowire in more detail we performed Density Functional Theory (DFT) based methods to solve the Schrödinger equation for the electrons in the system. DFT was first introduced by Hohenberg and Kohn in 1964 [15], when they proved the one-to-one relationship between the ground state electron density and the external potential of a given system. This work was extended by Kohn and Sham [20] to what is known as the Kohn-Sham ansatz, which reduced the problem of solving a many-body Schrödinger equation to a set of single electron equations that give the same ground state electron density as the full many-body equation. The Kohn-Sham equation for single electrons is given as:

$$\frac{-\hbar^2}{2m} \nabla^2 \psi_{n,\mathbf{k}} + v(\mathbf{r}, [n(\mathbf{r})]) \psi_{n,\mathbf{k}} = \epsilon_n(\mathbf{k}) \psi_{n,\mathbf{k}} \quad (32)$$

$$n(\mathbf{r}) = \sum_{n,\mathbf{k}} f(\epsilon_n(\mathbf{k})) \psi_{n,\mathbf{k}} \psi_{n,\mathbf{k}}^* \quad (33)$$

where $f(\epsilon_n(\mathbf{k}))$ is the Fermi function. The potential $v(\mathbf{r}, [n(\mathbf{r})])$ is a functional of the density $n(\mathbf{r})$ and is the sum of the ionic potential $v_{\text{ext}}(\mathbf{r})$, the classical coulomb potential $v_{\text{Hartree}}(\mathbf{r}, [n(\mathbf{r})]) = e/2 \int d^3\mathbf{r}' n(\mathbf{r}') / |\mathbf{r} - \mathbf{r}'|$ and the exchange-correlation potential functional $v_{\text{xc}}(\mathbf{r}, [n(\mathbf{r})])$. For periodic solids the solutions of the Kohn-Sham equation are in the form of Bloch waves. To solve the equation one starts with an initial guess for $n(\mathbf{r})$ and use it to construct the potential. Then Eq. 32 gives a set of states $\psi_{n,\mathbf{k}}$ and the new $n(\mathbf{r})$ is calculated

from these states. The updated density is used to construct a new potential, which is then fed back into Eq. 32. This loop is repeated until self-consistency is reached. At the end of the self-consistency cycle, we obtain the ground state density $n(\mathbf{r})$, the single electron wavefunctions $\psi_{n,\mathbf{k}}$ and the associated eigenvalues $\epsilon_n(\mathbf{k})$. From these we can deduce a rich set of information about the device, ranging from the density of states to the stress and forces in the structure. In this investigation we are interested in the properties of electrons, so the two most important properties we wish to obtain are the band structure and the projected densities of states.

The information about the band structure is already contained in the eigenvalues $\epsilon_n(\mathbf{k})$. With a local atomic basis set e_α , it is also easy to calculate the projected density of states. Each wavefunction $\psi_{n,\mathbf{k}}$ can be spanned by the atomic orbitals $\psi_{n,\mathbf{k}} = \sum_\alpha a_{n,\alpha}(\mathbf{k})e_\alpha$. The total density of states for a closed shell system can be defined as

$$g_{\text{tot}}(\epsilon) = \frac{2}{\Omega} \sum_n \int_{BZ} d^3\mathbf{k} \int d^3\mathbf{r} \psi_{n,\mathbf{k}}(\mathbf{r}) \psi_{n,\mathbf{k}}^*(\mathbf{r}) \delta(\epsilon_n(\mathbf{k}) - \epsilon) \quad (34)$$

$$= \frac{2}{\Omega} \sum_{n,\alpha,\beta} \int_{BZ} d^3\mathbf{k} a_{n,\alpha}(\mathbf{k}) a_{n,\beta}^*(\mathbf{k}) S_{\alpha\beta} \delta(\epsilon_n(\mathbf{k}) - \epsilon) \quad (35)$$

where Ω is the volume of the cell, $S_{\alpha\beta} = \int d^3\mathbf{r} e_\alpha e_\beta$ and there are 2 spins per state. The projected density of states onto to each atomic orbital $g_\alpha(\epsilon)$ and each atom $g_{\text{atom}}(\epsilon)$ can be obtained from:

$$g_\alpha(\epsilon) = \frac{2}{\Omega} \sum_{n,\beta} \int_{BZ} d^3\mathbf{k} a_{n,\alpha}(\mathbf{k}) a_{n,\beta}^*(\mathbf{k}) S_{\alpha\beta} \delta(\epsilon_n(\mathbf{k}) - \epsilon) \quad (36)$$

$$g_{\text{atom}}(\epsilon) = \sum_{\alpha \in \text{atom}} g_\alpha(\epsilon) \quad (37)$$

The total density of states provides us with the position of the resonance energies in the nanowire and their widths. The projected density of states onto a particular InAs or InP unit cell inside different parts of the nanowire gives us information on the contribution of different states to the electronic structure in these sub-regions. This also gives us a qualitative idea on the sharpness of the interface between InAs and InP.

For more information about the theory and techniques behind Density Functional Theory calculations, the book by R. M. Martin [26] and its references are recommended.

3.3.1 InAs and InP Structures Used For DFT Calculation

Both InAs and InP have zinc-blend structures (see Figure 12), which consists of two face-centered cubic (fcc) lattices off set by 0.25 of the lattice constant in each of the lattice vector directions. Due to time constraints of the project, we will only perform DFT calculations on a fixed ionic lattice, with the lattice parameters chosen to be the experimental lattice parameters for bulk InAs and InP. These are quoted as 6.058Å for InAs and 5.869Å for InP [14]. To study bulk electronic properties, we used periodic boundary conditions and the 2 atom primitive fcc cell for InAs and InP with the respective experimental lattice constants.

For the InAs-InP nanowires, we use periodic boundary conditions along the length of the wire. This is equivalent to assuming the wire is infinitely long with repeating InAs and InP sections. This does not model the device with finite number of barriers exactly, but will still provide us relevant information about the electronic structures in the InP barrier and InAs regions and at the interfaces. This is because the InP barriers are sufficiently wide to ensure that states in the InAs wells are well localized, and thus the interaction between neighboring wells is rather weak.

Because the nanowire is about 50nm in diameter, a DFT calculation including an entire cross-section of the device would be too expensive. Instead, we approximate the wire by treating it as a bulk structure, with periodic boundary conditions in both the transverse and longitudinal direction. We lose the influence of the wire surfaces, but provided the properties are dominated by the bulk this approach delivers useful information. To capture the bulk properties the (Bloch) \mathbf{k} space mesh used in the calculation must be fine enough in the transverse direction. Tests on bulk InAs and InP indicate a mesh of 8 k-points in the Brillouin

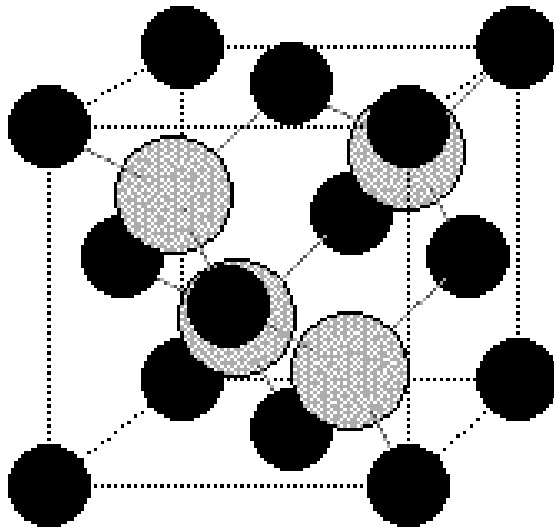


Figure 12: Zinc-blend structure.

zone along each of the lattice vectors in the transverse direction is sufficiently fine to generate bulk like properties.

To construct a unit cell for the nanowire, we used a 4 atom unit cell for both InAs and InP. To construct the unit cell, we applied the transformation

$$\mathbf{T} = \begin{pmatrix} 0.5 & -0.5 & 0 \\ 0.5 & 0.5 & 0 \\ 0 & 0 & 1 \end{pmatrix} \quad (38)$$

to the translation vectors of the standard zinc-blend 8 atoms unit cell. We then build up the unit cell for the device by attaching these InAs and InP cells along the z -direction (see figure 13). We looked at the InAs-InP junctions of various sizes. The 8 atom cell, which is the smallest InAs-InP junction we generated, has one InAs 4 atom unit cell and one InP cell along the longitudinal z -direction. In the 16 atom cell, the InAs and InP repeating sections are twice as long. For the 64 atom cell the device has InAs and InP sections each about 48.5\AA long. Finally the 128 atoms cell, which is designed to reproduce the setup of the experimental double barrier device, has a 48.5\AA InP barrier attached to a 145.392\AA InAs well. It is important to note that we used the experimental InAs lattice parameters for both InAs and InP regions in the wire. This is due to the fact that a full structure relaxation for a system as large as the 128 cell would be prohibitively expensive in our case. The difference in the experimental lattice parameter between InAs and InP is only about 3%, and in the real device the majority of the nanowire is made of InAs with only thin strips of InP barriers inserted into the wire. The use of the InAs experimental lattice parameter as the basic lattice parameter for each of the InAs/InP sub-cells is therefore reasonable.

3.3.2 The Choice of Exchange-Correlation Functional

Care has to be taken in choosing the appropriate exchange-correlation functional $v_{xc}(\mathbf{r}, [n(\mathbf{r})])$ for our DFT calculations. It is well known that both LDA (Local Density Approximation) and GGA (Generalized Gradient Approximation) functionals underestimate the band gaps [14, 29], and this is particularly problematic for semiconductors, whose gaps are usually very small. The cause of the problem in these approaches is due to the systematic error in the treatment of exchange for the electrons [12, 13, 17, 23–25, 28]. In particular

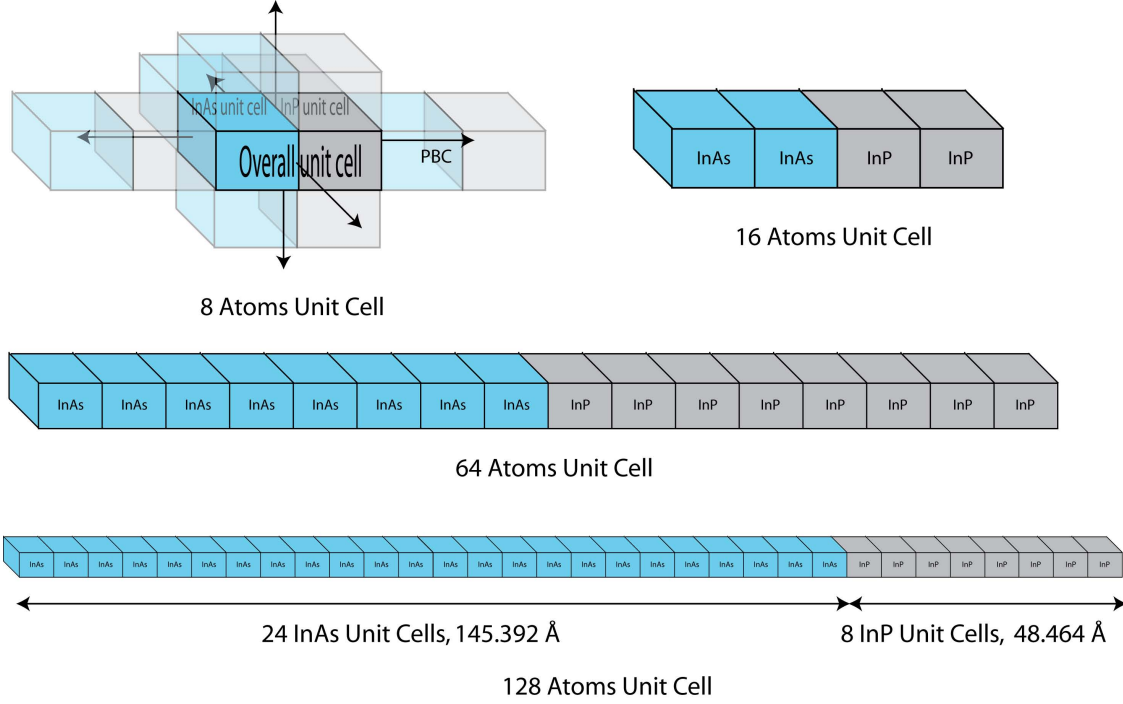


Figure 13: The unit cells we used in our DFT calculation. Each of the sub-cells of InAs (or InP) contains 4 atoms – 2 In and 2 As (or P). The periodic condition is demonstrated by the 8 atoms unit cell.

for InAs both LDA and GGA severely underestimates the energy of the bottom of the conduction band, and give zero band gaps. This is illustrated in Figure 14 where LDA was used to calculate the bands for bulk InAs using the computer program VASP³. This is also confirmed by results from other work [14, 34].

Thus neither LDA nor GGA is suitable for our calculations. However, hybrid functionals – which improve the treatment of exchange by combining (semi-empirically) exact Hartree-Fock exchange with exchange and correlation from GGA – are known to give much better descriptions of band structure in materials. It has been observed that both the B3LYP [31] and the HSE (Heyd-Scuseria-Ernzerhof) [14] hybrid functionals give adequate band gaps for both InAs and InP [14, 34]. We therefore decided to use the B3LYP functional for our DFT calculations. The computer program we used for the calculation is CRYSTAL, which is an *ab initio* simulation package for calculation of the ground state energy, energy gradient, electronic wavefunctions and properties of periodic systems. The B3LYP functional is implemented in CRYSTAL: for more information please refer to the package’s home page: <http://www.crystal.unito.it>

3.3.3 Spin-Orbit Contributions

Non-collinear spin-orbit contributions to the electronic structure becomes significant for heavier elements as the core electrons near the nucleus becomes relativistic. We investigated the effect of spin-orbit coupling on the electronic structure of InAs and InP to see if we can safely omit it from our DFT calculations. For a detailed analysis of spin-orbital contributions to various semiconductor compounds using hybrid functionals, we refer the reader to the paper by Peralta et al. (2006) [27].

We found that (see [27]) for both InAs and InP the spin-orbital contribution splits the originally three fold degenerate states at the Γ point at top of the valence band. The level of splitting is calculated to be 0.33

³VASP, the Vienna Ab-initio Simulation Package, is an ab-initio quantum-mechanical molecular dynamics code using pseudopotentials and plane wave basis sets developed by the VASP group of Universität Wien, Austria. For more information please visit <http://cms.mpi.univie.ac.at/vasp>

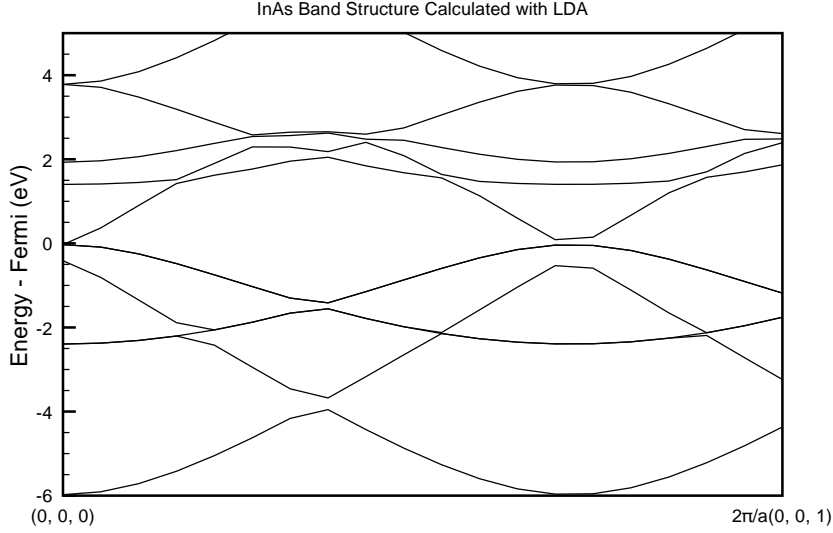


Figure 14: InAs bulk band structure calculated using LDA. Note that there is no band gap at the Fermi energy.

eV (0.38 eV experimental result) for InAs, and 0.08 eV (0.11 eV experimental result) for InP. The splitting is substantial especially for InAs, considering the gap is only about 0.4 eV. However there is no splitting reported at the bottom of the conduction band, which consists of just one state at Γ . As the main focus of our calculations is to obtain information about resonant states at the bottom of the conduction band in InAs-InP device, what matters for us is only the correct description of the bottom of the conduction band for both InAs and InP. Since all spin-orbit splittings happen at the top of valence band, it is a reasonable approximation for us to omit spin-orbit splittings from our calculations.

3.3.4 The Choice of Basis Set

CRYSTAL uses an atomic orbital basis set, which in turn is spanned by a linear combination of Gaussian functions. There are many different types of standard basis set available, and we compared several well known ones using calculations on the band structures of bulk InAs and bulk InP.

The basis sets we used in the test are described in table 5. We could only obtain the 6-331G* all electron basis set and its variants for P. However the all electron basis sets are always more accurate than the basis sets using pseudopotentials. The disadvantage of using an all electron basis is computational cost. However, as P has only 15 electrons, the computational cost is still manageable. Because no approximations are made on the ionic potentials, the all electron basis sets are compatible with other pseudopotential basis sets.

Table 6 shows the results we obtained for InAs and InP bulk using the different available of basis sets. It was observed, as expected, that in general the non-modified basis sets give a slightly more accurate description of the band structure, and a lower total energy. However, due to the inclusion highly diffuse Gaussian functions, these basis sets are computationally more expensive, and can produce numerical instability. The numerical stability becomes worse as the system size increases. Comparing results from the Tomić version of the m-pVDZ-PP basis set and the standard m-pVDZ-PP basis set, the Tomić basis set gives a slightly lower total energy. However the standard m-pVDZ-PP basis set gives a slightly better description of the band gap. As a good description of the band gap is important for us, we decided to use the standard m-pVDZ-PP basis set for both In and As, and the m-6-331G* all electron basis set for P.

6-331G*	A standard all electron atomic orbital basis set (made by linear combination of Gaussians). No pseudopotential.
m-6-331G*	Same as 6-331G* basis set except that Gaussian functions with the exponent less than 0.12 a.u. are omitted. This reduces the number of Gaussians which are too diffuse in the basis and improves on convergence and numerical stability.
pVDZ-PP	A standard pseudopotential basis set, which takes one shell (including all angular momentum orbitals) below the valence shell as the semi-core electrons and regards the rest as core electrons. Relativistic corrections are added.
m-pVDZ-PP	Same as pVDZ-PP, but with the Gaussians having exponents less than 0.12 a.u. omitted.
Tomić	Same as m-pVDZ-PP however with exponent of the Gaussian for one of the empty s-orbitals of In being replaced by the value of 0.25 a.u. from the original 0.170415 a.u. ^a This is done to make the orbital more linearly independent to the other s-orbital which is given with Gaussian coefficient of 0.12 a.u. due to the omission of Gaussians with exponents less than 0.12 a.u.. This improves numerical stability.

^aPrivate communications with the authors of [34].

Table 5: The basis sets for CRYSTAL available to us for our calculations.

	In Basis set	As Basis set	ΔE (eV)	Band-gap at Γ (eV)
InAs bulk	pVDZ-PP	pVDZ-PP	0.0000	0.3859
	m-pVDZ-PP	pVDZ-PP	0.0252	0.5581
	pVDZ-PP	m-pVDZ-PP	0.0072	0.3785
	m-pVDZ-PP	m-pVDZ-PP	0.0815	0.5249
	Tomić	m-pVDZ-PP	0.0635	0.5546
	Experiment		–	0.42
	In Basis set	P Basis set	ΔE (eV)	Band-gap at Γ (eV)
InP bulk	pVDZ-PP	6-331G* ^a	0.0000	1.6116
	m-pVDZ-PP	6-331G*	0.0484	1.7342
	pVDZ-PP	m-6-331G*	-0.0033	1.5859
	m-pVDZ-PP	m-6-331G*	0.0424	1.6806
	Tomić	m-6-331G*	0.0307	1.7570
	Experiment		–	1.42

^aNote that for numerical stability, one of the Gaussian exponent smaller than 0.12 a.u. for P has already been removed.Table 6: Comparison between different basis sets. ΔE is the change in total energy with basis set relative to that for the pVDZ-PP basis set.

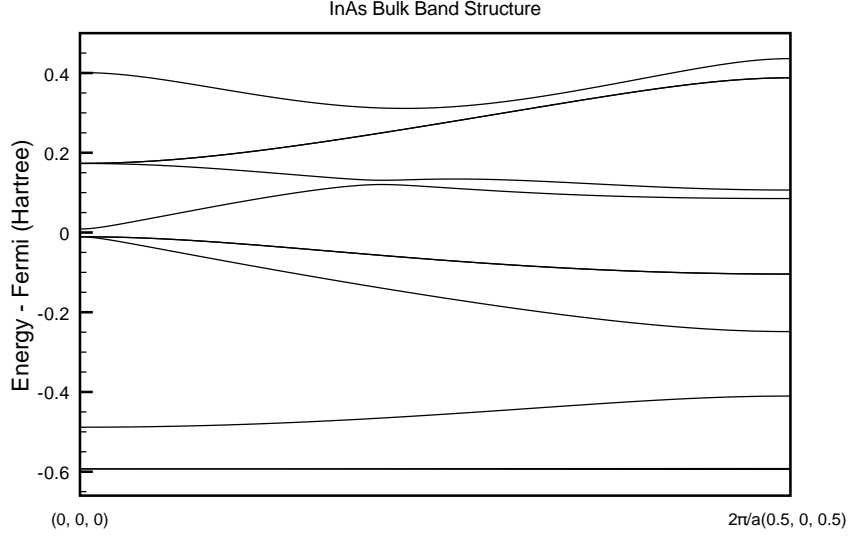


Figure 15: Band structure of bulk InAs along the line Γ to X . Note that the primitive unit cell is used.

4 Results and Discussions

We now report on the results of our calculations using both Density Functional Theory and our device simulator. Results found using the simulator allow us to propose a specific device that might be tested experimentally. We find that the DFT calculations support the basic picture employed by the device simulator.

4.1 Density Functional Theory Calculations

4.1.1 InAs and InP Bulk

Figures 15 and 16 show the CRYSTAL calculated band structure and the projected densities of states for bulk InAs. Figures 17 and 18 shows the band structures and projected densities for bulk InP. The band structures are plotted along the line in Bloch space $\mathbf{k} = \Gamma = (0, 0, 0)$ to $X = \frac{2\pi}{a}(\frac{1}{2}, 0, \frac{1}{2})$ in the reciprocal lattice coordinates: this corresponds to a line from $(0, 0, 0)$ to $\frac{2\pi}{a}(0, 1, 0)$ in Cartesian coordinates. Here a is the lattice parameter in the z -direction, and for bulk calculations this is the experimental lattice parameters for InAs and InP (6.058\AA and 5.869\AA) respectively. Due to the symmetry of the bulk, there should be no difference between $(0, 1, 0)$ and $(0, 0, 1)$ directions in Cartesian coordinates.

The band gap for bulk InAs is measured at the Γ point to be 0.52 eV, and the gap for bulk InP is measured also at the Γ point to be 1.68 eV. The difference in the gaps is thus 1.16 eV, which compares favorably with the experimental result of about 1.0 eV [14, 27, 34]. Also noticeable for both InAs and InP are the three-fold degenerate states at the top of the valence band at Γ point. They are the three degenerate p-like orbitals, which will become non-degenerate if we had included spin-orbit splitting. However, there is only one state at the bottom of conduction band. This supports our argument for omitting the spin-orbit contributions.

4.1.2 InAs-InP Nanowires

We calculated the projected densities of states and band structures for the 8 atom unit cell, the 16 atom unit cell, the 64 atom unit cell and the 128 atoms unit cell InAs-InP nanowires (see figure 13). The band structures are plotted from $\mathbf{k} = \Gamma$ to the second Brillouin zone boundary in k_z direction at $\frac{2\pi}{a}(0, 0, 1)$ in

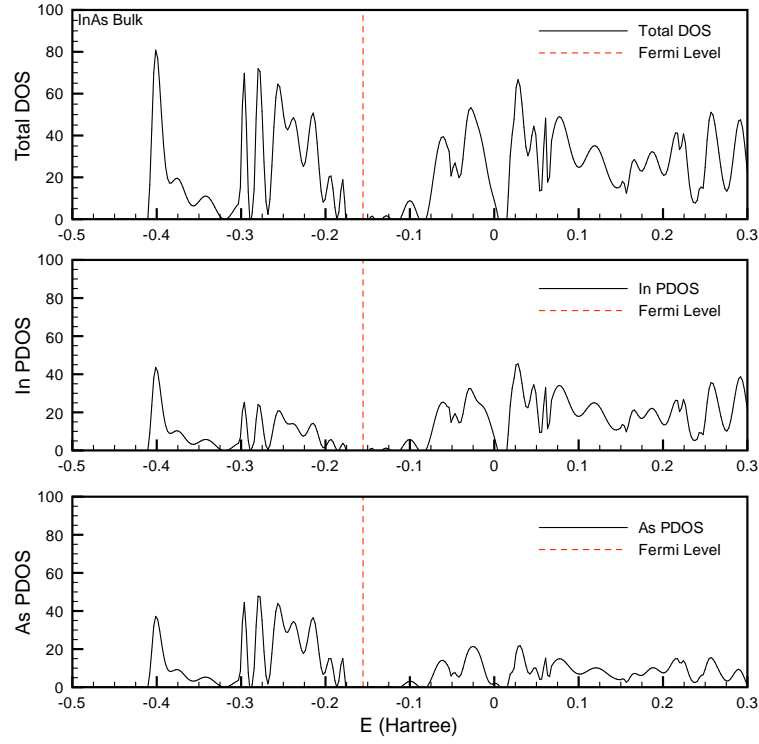
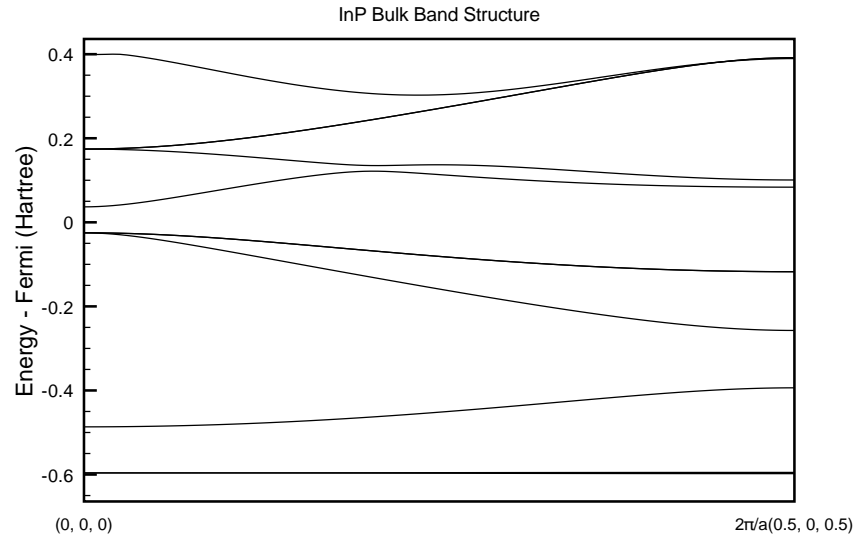


Figure 16: Total and projected densities of states for bulk InAs.

Figure 17: Band structure of bulk InP along the line Γ to X . Note that the primitive unit cell is used.

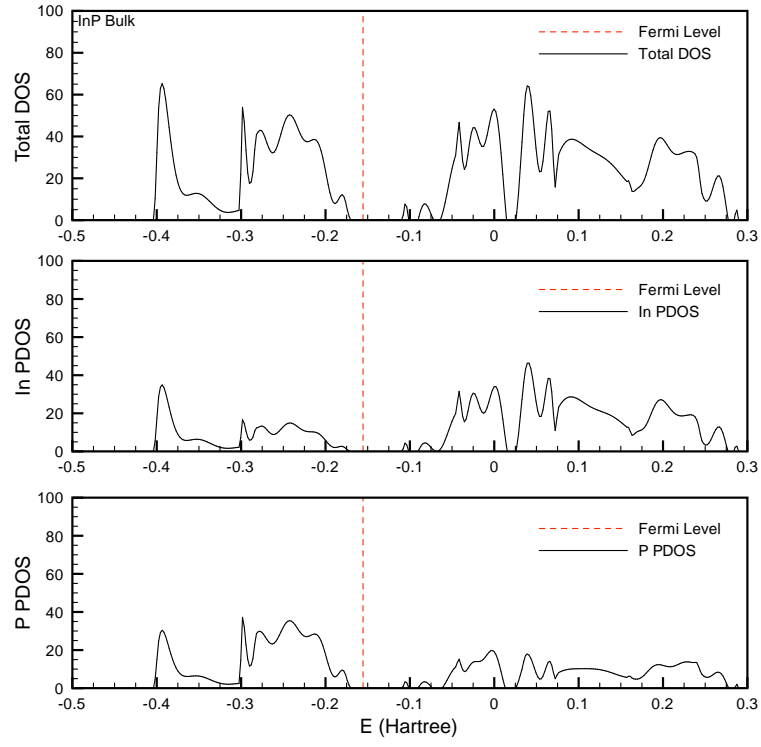


Figure 18: Total and projected densities of states for bulk InP.

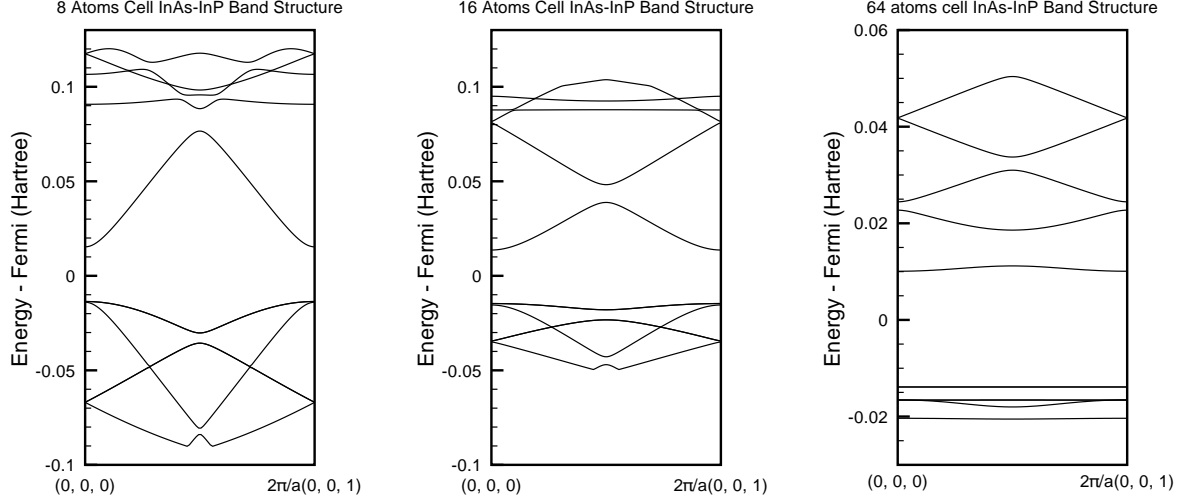


Figure 19: Band structures of InAs-InP nanowire having repeating units of 1 InAs unit cell and 1 InP unit cell (8 atoms unit cell), 2 InAs and 2 InP (16 atoms) and 8 InAs and 8 InP (64 atoms) respectively.

Cartesian coordinates. Here a is the length of the unit cell along z -direction. This means $a = 12.116\text{\AA}$, 24.232\AA , 96.928\AA and 193.856\AA for the 8, 16, 64 and 128 atoms unit cell calculations respectively.

Going from the 8 atom unit cell calculation to the 64 atoms unit cell calculation, the lengths of InAs well and the InP barrier increase. If one can approximate the well-barrier device as a periodic system of square wells, then one would expect that reducing the width of the wells would push the discrete resonance states in the well apart and raise the energy of lowest resonance (see below). A narrower potential barrier allows more tunneling between wells, thereby increasing the contribution of states from other wells to its resonance states, making them broader. This is demonstrated from the comparison of band structure plots for the 8, 16 and 64 atoms unit cell calculations shown in figure 19. As the well and barrier widths increase, the bands “squeeze” together, and the lowest conduction band narrows significantly, this being particularly evident for the 64 atom unit cell nanowire. This very narrow band corresponds to a resonant state in the InAs well.

To study the resonances in more detail, we looked at the projected densities of states for the 64 atoms unit cell system (see Figures 20, 21 and 22). The densities of states are calculated by sampling 30 k -points in the Brillouin zone along k_z -direction from Γ point. We need many points along the direction in Bloch space corresponding to the longitudinal direction of the wire because it is the bottom tip of the conduction band that is most important to conduction in the device, and it needs to be described accurately. On the other hand, due to the symmetry of the nanowire in the transverse direction, states corresponding to different k -points in the transverse direction can be regarded as independent channels. We are thus able to look at one channel at a time by sampling lines along the k_z direction starting from different k -points in the transverse directions. As the number of charge carriers in the device will be very low, and because the Γ point has the minimum energy at the bottom of the conduction band, it is expected that most relevant channel for the device would be the Γ channel. For the projected densities of states, we project the total density of states (see equation 37) onto the a set of sub-unit cells of 4 atoms each corresponding to the unit cells of InAs (or InP) in the middle of each well (or barrier) region and at the interface.

From the projected density of states plots (figures 20, 21 and 22), for the 64 atoms system, we observe one narrow state is formed at the bottom of the conduction band, and three narrow bands are formed at the top of the valence band. The narrow peak at the bottom of the conduction band can be understood as a resonance state inside the InAs well. The narrow peaks at the top of the valence band indicates that in the InAs-InP nanowire, the InAs region not only has a lower conduction band, but also a higher valence

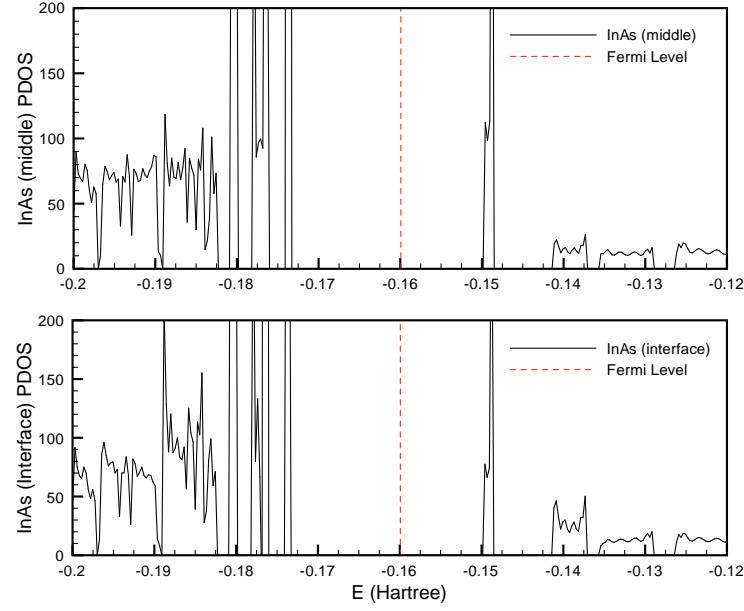


Figure 20: The projected densities of states from the 64 atoms unit cell calculation for the InAs unit cells at the middle of InAs region and at the interface of the nanowire device.

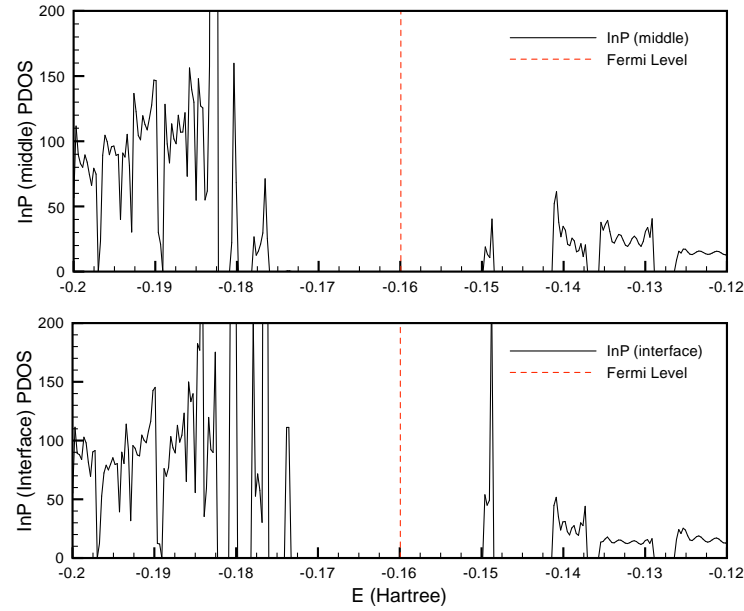


Figure 21: The projected densities of states from the 64 atoms unit cell calculation for the InP unit cells at the middle of InP region and at the interface of the nanowire device.

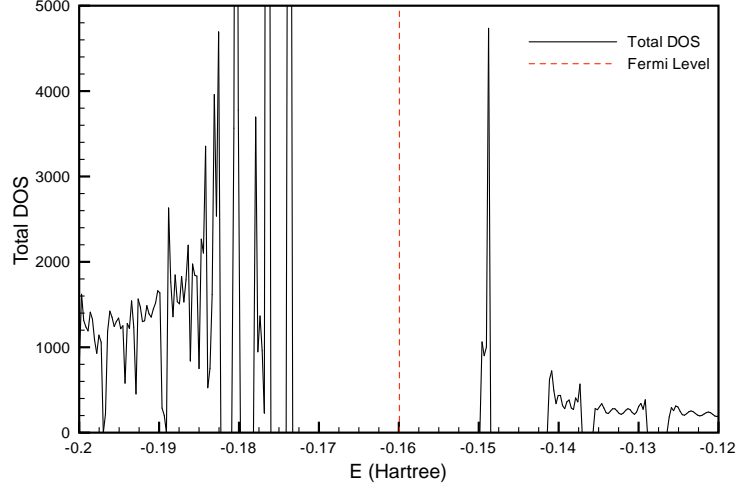


Figure 22: The total density of states from the 64 atoms unit cell calculation.

band than the InP region (as is illustrated in Figure 5). The states at the top of the valence bands do not have a corresponding state of the same level in the InP region, and this forms an effective barrier for the electrons just as is the case for the bottom of the conduction band. It may be helpful to picture this as a potential barrier at the bottom of conduction band for holes (for holes the band structure is up-side-down). The drop in the height in the resonance peaks as we move from the interface to the middle of the InP region (Figure 21) indicates that the magnitude of the resonance wave functions starts to drop in the barrier, as expected. As these peaks remain throughout the InAs region, it is further evidence that these peaks are indeed resonance states formed at the bottom of the InAs well. The width ΔE_0 of the resonance peak at the bottom of conduction band for the 64 atoms unit cell device can be measured directly from the total density of states, and $\Delta E_0 = 0.037$ eV.

Figures 23, 24, 25 and 26 show the band structure and projected densities of states calculated for the 128 atoms unit cell nanowire. The difference in the setup between the 128 atom unit cell system and the 64 atom unit cell case is the width of the InAs well. They both have InP barriers with width of 48.5\AA , but the 128 atom unit cell nanowire has three times the width of the well as the 64 atom case. The difference in the electronic properties caused by widening the well width can be observed from the projected densities of states plots. The 128 atom unit cell system case has more narrow states at the bottom of conduction band and top of the valence band. As one increases the well width the separation between the discrete resonance states decreases (in the case of infinite square the separation between resonances is inversely proportional to the square of the well width). The widths of the narrow resonance states however did not change much for the 128 atoms unit cell case: $\Delta E_0 = 0.022$ eV, $\Delta E_1 = 0.019$ eV and $\Delta E_2 = 0.034$ eV for the three resonance states from the bottom of the conduction band. This is because the width of the resonances is determined by the width of the barrier.

One way to estimate the band offsets is from the average potential in the heterostructure as a function of position[21]. However, time has not permitted this to be done. We just note that the presence of sharp resonances at the band edges of the heterostructures indicates that the band offsets are at least qualitatively as expected as they are generating the relevant effective barriers.

The rate of which the the resonance peaks drop in height from the interface region of InP into the the middle of the barrier gives a qualitative measure of how hard (i.e. how square the well is) the InAs-InP interface is. For a strictly square well, the amplitude of wavefunctions is expected to drop exponentially with respect to z . A softer interface would result in the peaks to drop in a slower pace as we move into the barrier.

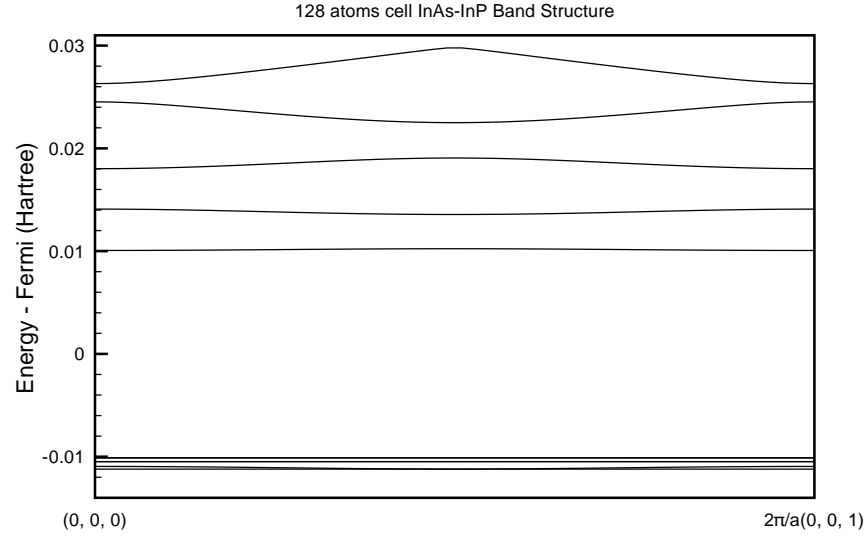


Figure 23: Band structure of the 128 atoms unit cell InAs-InP nanowire.

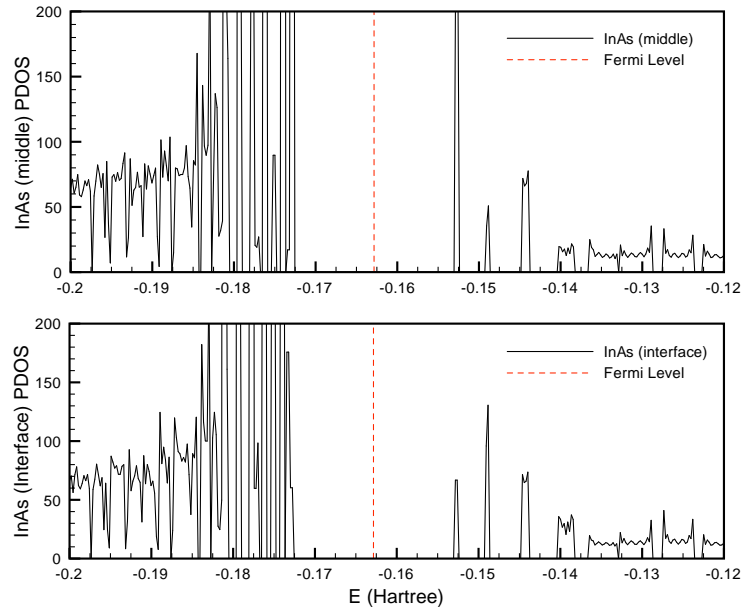


Figure 24: The projected densities of states from the 128 atoms unit cell calculation for the InAs unit cells at the middle of InP region and at the interface of the nanowire device.

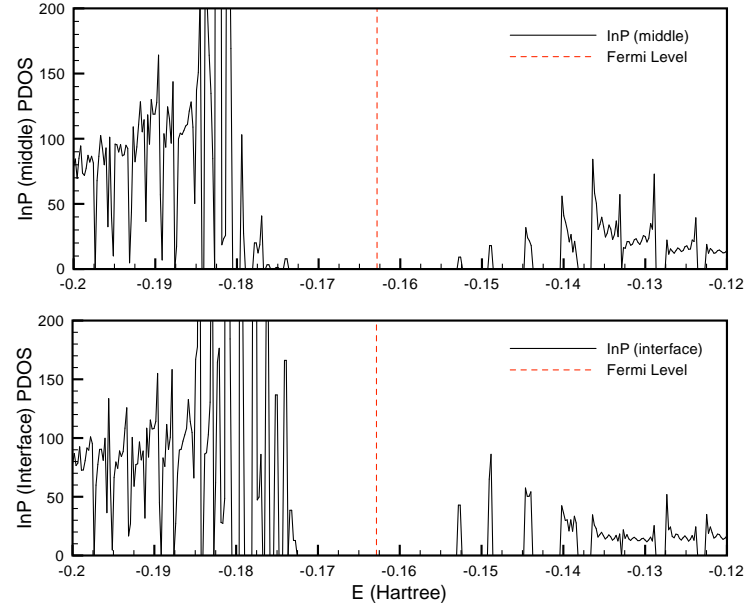


Figure 25: The projected densities of states from the 128 atoms unit cell calculation for the InP unit cells at the middle of InAs region and at the interface of the nanowire device.

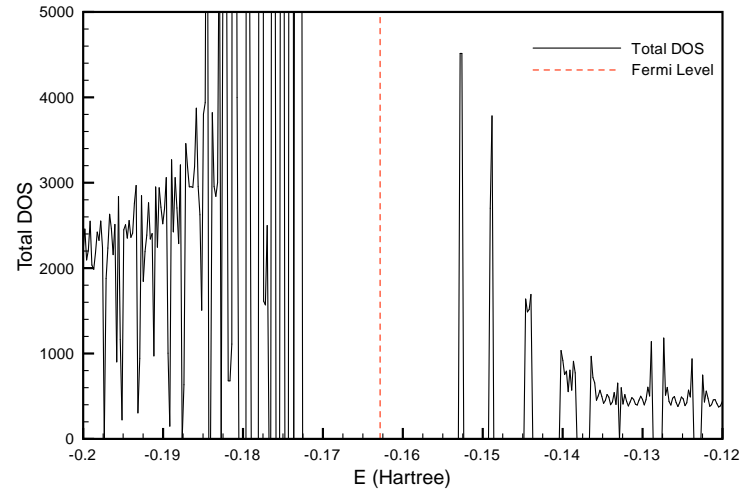


Figure 26: The total density of states from the 128 atoms unit cell calculation.

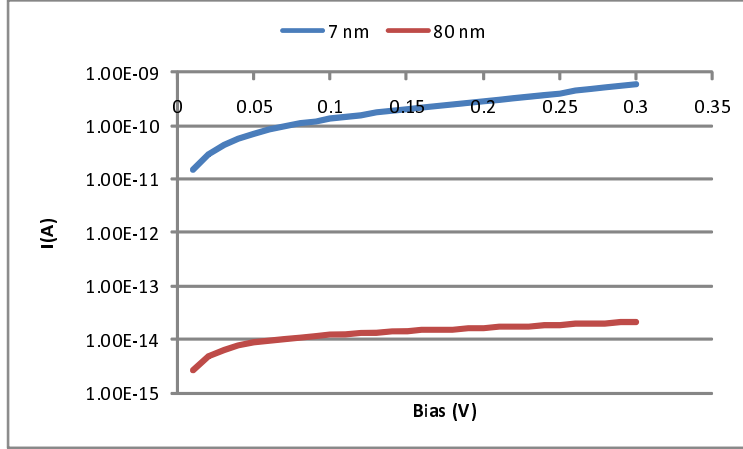


Figure 27: Current versus voltage for two single barrier devices at room temperature. The blue curve corresponds to a barrier width of 70\AA , and the red curve to a barrier width of 800\AA . A carrier concentration of 10^{-7-3} was assumed, and temperature is 300K .

4.2 Effective mass approximation calculations

First we use our device simulator to reproduce the experimental results of Björk[4] shown in Figure 4 as a way to validate our model. The experiments involve devices with one barrier and with two barriers (one well). We then use the simulator to predict properties of the two well (three barrier) device that we wish to use as a chemical sensor.

4.2.1 Single barrier devices

The results shown in Figure 27 are to be compared with the left panel of Figure 4. We see good qualitative agreement between the theoretical and experimental results, notably the four orders of magnitude increase in current on going from the thin barrier to the thick barrier. Also the exponential dependence of the current on the bias is clearly visible in both cases. For the theoretical calculations we used a carrier concentration of 10^{-7-3} , which is an order of magnitude greater than our previous estimate based on the conductivity of a barrier free wire. Even so, our currents are still a little smaller than the experimental ones. The origin of this discrepancy is not fully understood, though there are a number of possible causes, including uncertainties in the dimensions of the device, and the effect of roughness at the interfaces.

4.2.2 Double barrier devices

We now consider a resonant device obstructed using two barriers with a well in between. The barriers have a thickness of 50\AA , and the well has a width of 150\AA . Comparing Figure 28 with the experimental data in the right panel of Figure 4, we see that our calculated currents are somewhat greater than the experimental, and the width of the resonances somewhat larger. By reducing the carrier concentration to $5 \times 10^{-9-3}$ we get fairly close to the experimental result. Once again we note that there are discrepancies that are hard to fully account for because of a number of features that are hard to introduce into the model (such as roughness), or are not precisely defined in the experiments (such as the precise thicknesses of the barriers and well). However, we view the level of agreement as sufficiently encouraging to allow simulations to be used to suggest working devices.

It is possible on the basis of the calculations to offer an explanation for the shape of the resonance observed. From Figure 28 we see that the position of the left-hand edge of the resonant profile is sensitive to the carrier concentration, while its width is not. This edge corresponds to a bound state in the well moving down under the influence of the bias until it overlaps with the tail of the Fermi-Dirac distribution of the

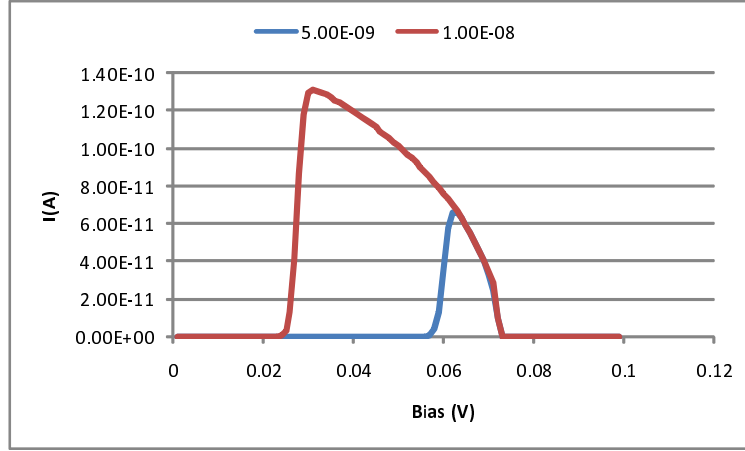


Figure 28: Current versus voltage for a double barrier device at 4.2K for two carrier concentrations. The red curve corresponds to a carrier concentration of 10^{-8-3} and the blue curve to $5 \times 10^{-9-3}$.

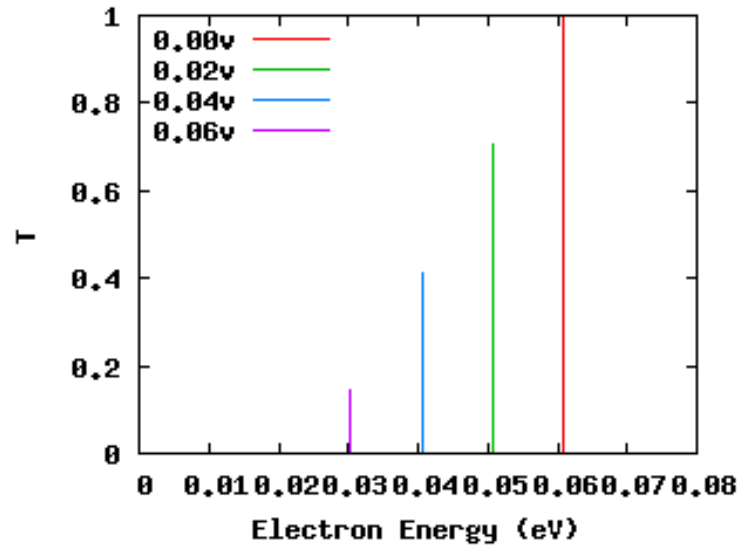


Figure 29: This figure shows the transmission probability as a function of energy for a range of bias voltages. A delta function approximation to the transmission is good, with the peak transmission being strongly dependent on voltage.

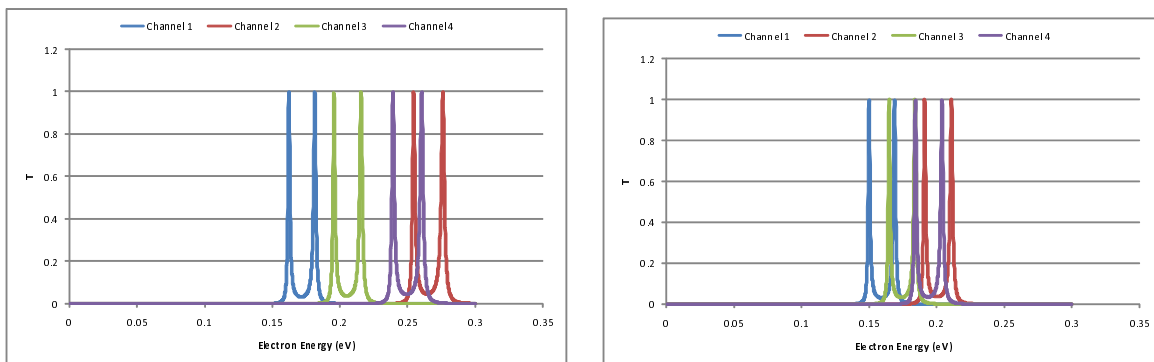


Figure 30: This figure shows how the transmission varies as the wire radius is increased from 200 Å (left) to 300 Å (right).

electrons in the left-hand lead. Therefore the width of the left edge is governed by the electron temperature, which is the same for both profiles. The position of the edge is defined by the chemical potential of the electrons in the left-hand lead, which increases as the doping levels increase. Thus we see the reduced bias required for a current flow when we increase the carrier concentration.

The right-hand edge is defined by the bias at which the bound state in the well drops below the band edge in the left-hand lead, which is why it is independent of the carrier concentration. Between the two edges there is a steady drop in the current. This is because of the reduced transmission through the device induced by the applied bias. The transmission through the lowest bound state as a function of the applied bias is shown in Figure 29. There we see a steady reduction in the transmission as the bias is increased.

4.2.3 Triple barrier devices

Here we consider the properties of the full device. The purpose is to identify a set of wire, barrier and well widths, and a dopant density that together constitute a promising candidate device to be tested experimentally.

Wire thickness

The radial part of the electronic wavefunctions is quantized, and defines channels (for elastic transmission) as it is invariant as the electron travels down the wire. The minimum energy for a given channel is set by the radius of the wire, thus the main effect of making the wire narrower is to increase the spacing between channels: this can be seen from Figure 30 where the transmission channels are much more closely spaced for a wire of radius 300 Å than for a wire of radius 200 Å. There is also a slight shift down in energy of the resonances as the wire radius is increased. It is unclear precisely how large we require the splitting between channels to be. The criterion is that it must be large enough to prevent excitation between channels within a given well. However, the ability for electrons to switch channel will depend on the nature of the coupling to the odorant. Clearly, the bigger the splitting, the safer we are. Furthermore, narrower wires (which generate larger splittings) have stronger coupling of the odorant to the electrons inside the wire as the distances involved are smaller. So on both counts we would like the wire to be as thin as possible. 200 Å is probably a reasonable target for current technology[3].

Outer Barriers

The main influence of the outer barriers is to set the width of the resonances in the wells. The broadening is due to the interaction of the resonances with the continuum of states in the leads. From Figure 31 we see that the peaks keep their positions but narrow substantially as the outer barrier widths are changed from 10 Å to 20 Å. The width of the resonances determines the resolution of our device: the wider the resonance, the larger the bias that needs to be applied to suppress elastic transmission through the device, and consequently the larger the difference in vibrational frequency between two molecules that is needed in order for them to be discriminated. However, making the resonances narrow reduces the electric current that can pass through

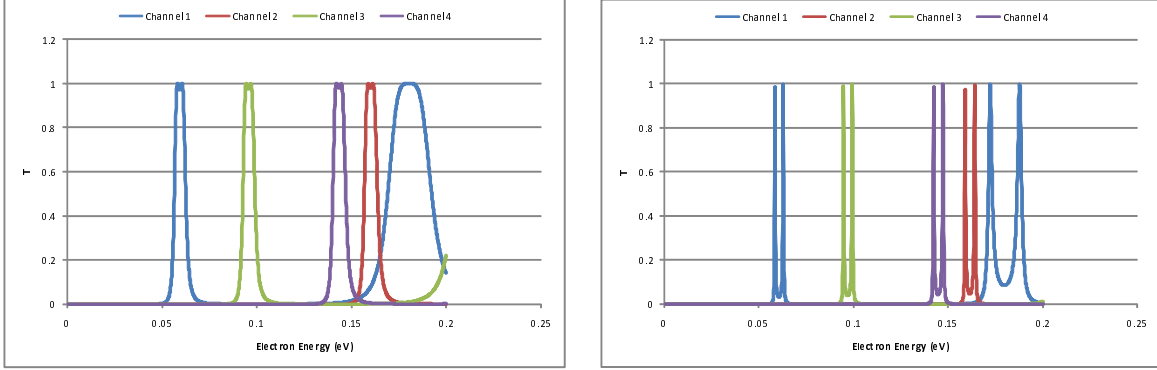


Figure 31: These figures show the effect of varying the *outer* barriers. Plotted is the variation of electron transmission with respect to the energy of the incident electron with no bias applied. The well width is 150\AA and the middle barrier width is 20\AA in both cases. In the left panel the outer barrier width is 10\AA while in the right panel it is 20\AA .

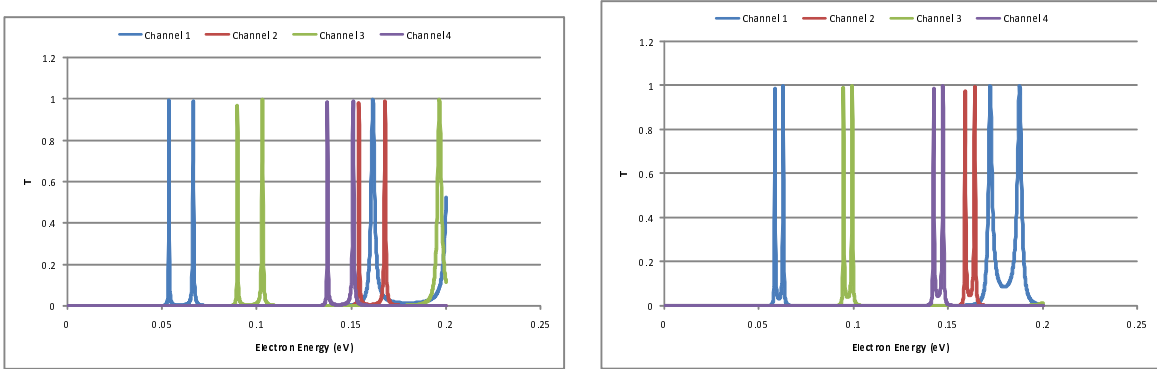


Figure 32: These figures show the effect of varying the *middle* barrier width. Plotted is the variation of electron transmission with respect to the energy of the incident electron with no bias applied. The well width is 150\AA and the outer barrier width is 20\AA in both cases. In the left panel the middle barrier width is 10\AA while in the right panel it is 20\AA .

the device. Thus a compromise is needed between sufficiently wide resonances (narrow outer barriers) to support a measurable current, and sufficiently narrow resonances to enable discrimination of molecules. For resolution purposes (see Table 1) we would like the resonances to have a width no larger than 0.01eV . From Figure 31 a barrier width of 20\AA looks sufficient. However, as we shall see below when we compute the I-V curves, a slightly wider barrier is needed.

Middle Barrier

The main influence of the middle barrier is to control the interaction of the localized states in each well with each other. This interaction is seen as a splitting of the peaks in the transmission: the larger the splitting, the greater the interaction. This is due to the formation of bonding and anti-bonding combinations of the resonance wavefunctions when they overlap slightly. From Figure 32 we see that increasing the middle barrier width from 10\AA to 20\AA reduces the splitting considerably. Since the splitting influences the resolution of the device, we need it to be smaller than the tolerance we are imposing (0.01eV). From Figure 32 we see that a middle barrier width of 20\AA is barely sufficient. Increasing the central barrier width to 25\AA brings the splitting down to 0.0025 eV , which is adequate.

Wells

The width of the wells determines two important parameters: the separation between the resonances

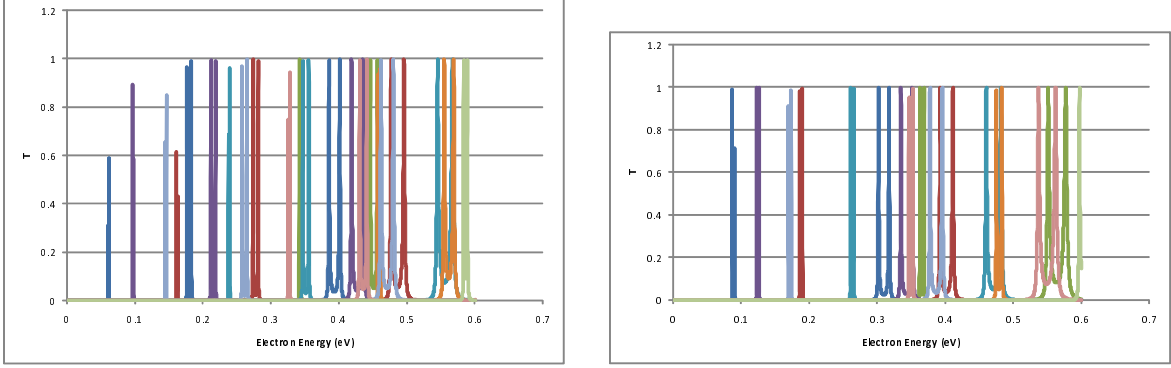


Figure 33: These figures show the variation of electron transmission with respect to the energy of the incident electron with no bias applied. All the barrier widths are 30\AA in both cases. In the left panel the well width is 150\AA while in the right panel it is 100\AA . Note that the maximum transmission in each channel should be 1. The apparent drop in maximum transmission below 1 in the left panel is a result of a lack of resolution of the plots.

Dopant Density (\AA^{-3})	Chemical Potential (eV)
10^{-8}	0.011
10^{-7}	0.12
10^{-6}	0.73

Table 7: Variation of electron chemical potential with dopant density at room temperature.

and the energy of the lowest resonant state. Note that the splitting between *channels* is not effected as this is set by the radius of the wire (see above). We require the separation between resonances to be larger than the vibrational energies of the molecules we would like to detect (of order 0.1eV) in order to prevent vertical transitions within a well. This requirement sets a maximum width for the wells (the wider the well, the narrower the spacing). Note that this requirement is made more complicated by the fact that different resonances belong to different channels, so transitions will only be possible if the coupling to the oscillating molecules couples electrons to transitions between these channels. We also require the lowest resonant state to have an energy sufficiently low that it can be populated by electrons from the lead (which depends on the electron chemical potential and hence dopant density - see Table 7). This sets a minimum width for the wells (the narrower the well, the higher in energy the lowest resonance).

Both effects are visible in Figure 33. All three barriers are given a width of 30\AA . We see that on decreasing the well width from 150\AA to 100\AA the lowest resonance shifts from about 0.06eV to about 0.087eV (a change of about 0.03eV - *c.f.* Table 4), and the density of resonances decreases at the lower energies. The most interesting feature is the opening up a gap in transmission above 0.2eV which could produce improved resolution. In both cases that there will be difficulties with charge injection with typical dopant densities which result in carrier densities of order 10^{-8-3} (see Table 7). It may be possible to overcome this problem by the application of a gate bias (see below). However, it strongly suggest that the wells should not be made any narrower than 100\AA .

Influence of the bias on transmission

In the absence of a bias, provided the two wells are equivalent, there will be energies at which an incoming electron encounters bound states in both wells with the same energy, thereby providing a high transmission path through the whole device. When a bias is applied to our device, the potential in the left and right wells start to differ from each other. If the bound states in the wells were totally uncoupled from each other, then these would shift apart in energy as the potential differ. Thus an electron will in general no longer encounter states in both wells with the same energy, and the transmission will drop substantially. This can be seen by

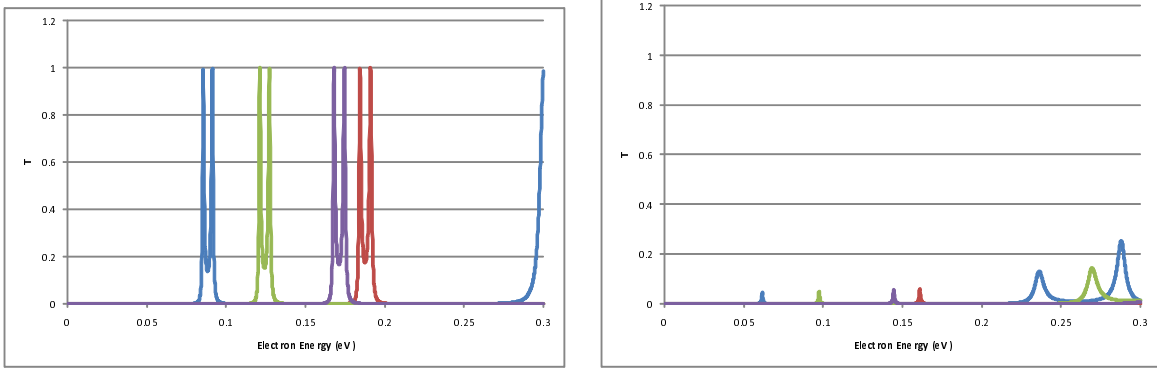


Figure 34: These figures show the transmission as a function of the electron energy, and refer to a nanowire with outer barrier widths of 20\AA , center barrier width of 25\AA , and well widths of 100\AA . In the left panel the bias is zero, while in the right panel the bias is 0.1V .

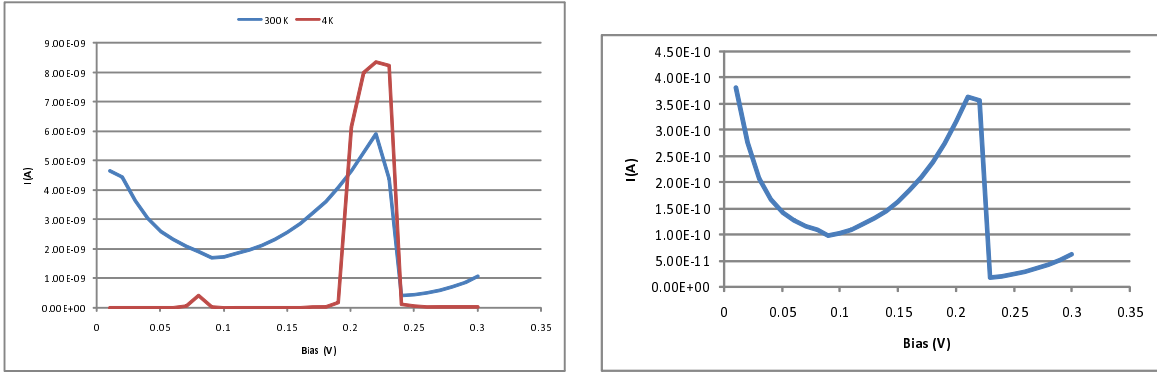


Figure 35: These figures show the variation of electric current with bias. The left panel has results at two temperatures (4K and 300K), and refers to a nanowire with outer barrier widths of 20\AA , center barrier width of 25\AA , and well widths of 100\AA . The right panel has results for 300K with wider barriers (all 30\AA).

comparing the left panel (zero bias) and right panel (bias of 0.1V) in Figure 34. If there is a molecule nearby with a vibrational frequency f such that hf equals the offset in energy of bound state, then an exchange of energy between the electron and that vibrational mode can restore resonance. However, the transmission will still be well below 1 because the probability of the electron exciting the molecule is generally much less than 1.

Temperature

It is very important that our device operate properly at room temperature. Indeed this is the reason for introducing two wells to filter the electron energy. Increasing the electron temperature broadens the range of states populated by electrons in the leads, which causes broadening of the I-V curve. From the left panel in Figure 35 we see that at low temperature (4K) there is a single significant peak in the current at a bias of about 0.22V . This corresponds to when the resonances are brought low enough by the bias to allow electron injection, but the bias is not yet big enough to completely disrupt the resonance itself (see above). At 300K we see a drop in the current at low voltages as the bias increases because the resonances in the two wells are moving out of alignment. This is what we require for inelastic tunneling spectroscopy so that the presence of an oscillating molecule possessing a mode with a frequency that matches the splitting between the resonance levels can produce an increase in current, and hence be detectable. As the bias increases, the current picks up again as more resonances become available, and then drops off sharply as the resonances drop below the

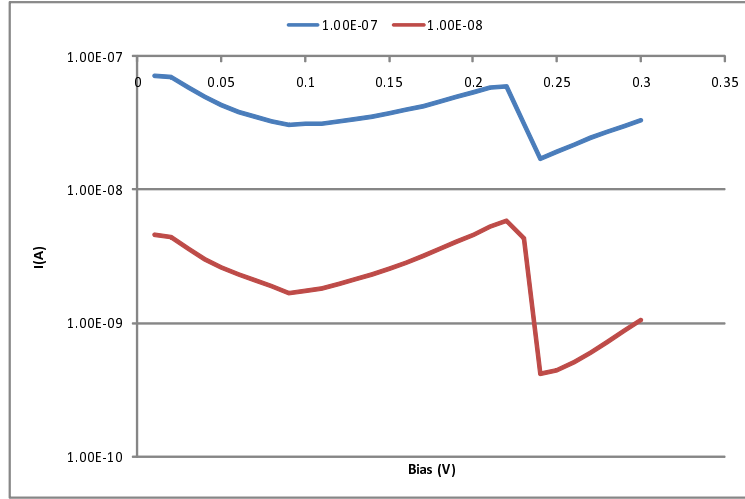


Figure 36: This figure displays the current as a function of voltage for two values of the carrier density in the leads. There is roughly factor of 10 increase in the current for a factor of 10 increase in the carrier density. All calculations are at 300K with well widths of 100Å, outer barrier widths of 20Å, and middle barrier width of 25Å.

energy of the incoming carriers.

At 4K the resolution of the device is of order 0.05eV, whereas at 300K it is closer to 0.1eV. As discussed above, this is not sufficient. In the right panel of Figure 35 we show the I-V curve at 300K with wider barriers (all 30Å). The resolution is improved (the current drops off faster with increasing bias), though still below the threshold we would ideally like. The current has dropped by an order of magnitude as well, so there is a high price for this increased resolution.

Carrier Density

The higher the dopant density the higher the electron chemical potential in the leads, and consequently the easier it is to populate the resonant states in the wells. The I-V curves in Figure 36 are for nanowires at 300K with well widths of 100Å, outer barrier widths of 20Å, and a middle barrier width of 25Å. We see that there is roughly factor of 10 increase in the current for a factor of 10 increase in the carrier density, with no obvious loss of resolution following from the increased carrier density. Note that for configurations with narrower wells (and hence localized states at higher energy) the ratio of increased current to increased carrier concentration can be much higher because of the exponential variation of carrier concentration with energy far above the chemical potential.

5 Conclusions

From the above we conclude that a promising device would have outer barrier widths of 30Å, a middle barrier width also of 30Å, and well widths of 100Å. A dopant density of 10^{-7}Å^{-3} looks good, but probably cannot be obtained by the natural carbon doping. It might be possible to increase the carrier density in the active region (where the wells and barriers are) by the application of a gate voltage[11]: see Figure 37. Note the gate will have to extend under the leads for a distance greater than the electron inelastic mean free path to ensure that carriers are thermalized near the barriers.

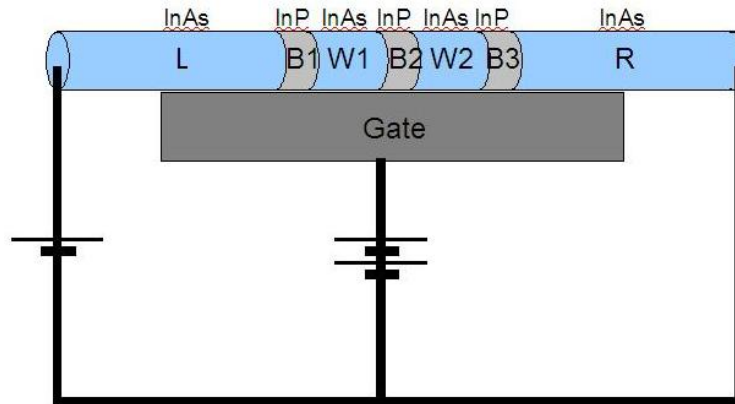


Figure 37: A cartoon indicating the use of a gate to increase the density of carriers in the active region.

References

- [1] C. J. Adkins and W. A. Phillips. Inelastic electron tunnelling spectroscopy. *J. Phys. C: Solid State Phys.*, 18:1313–1346, 1985.
- [2] G. Baym. *Lectures on Quantum Mechanics*. Benjamin/Cummings, 1973.
- [3] M. T. Bjork, B. J. Ohlsson, T. Sass, A. I. Persson, C. Thelander, M. H. Magnusson, K. Deppert, L. R. Wallenberg, and L. Samuelson. One-dimensional heterostructures in semiconductor nanowhiskers. *Applied Physics Letters*, 80(6):1058–1060, 2002. article Compaq_Owner.
- [4] M. T. Bjork, B. J. Ohlsson, C. Thelander, A. I. Persson, K. Deppert, L. R. Wallenberg, and L. Samuelson. Nanowire resonant tunneling diodes. *Applied Physics Letters*, 81(23):4458–4460, 2002. article Compaq_Owner.
- [5] V. Bommisetty, S. Bhandari, R. L. Karmacharya, D. A. Rislov, R. D. Mileham, and D. W. Galipeau. Gas sensing based on inelastic electron tunneling spectroscopy. *IEEE Sensors Journal*, 8(6):983–988, 2008.
- [6] J. C. Brookes, F. Hartoutsiou, A. P. Horsfield, and A. M. Stoneham. Could humans recognize odor by phonon assisted tunneling? *Physical Review Letters*, 98:038101, 2007.
- [7] A. Deisingh, D. Stone, and M. Thompson. Applications of electronic noses and tongues in food analysis. *International Journal of Food Science and Technology*, 39:587–604, 2004.
- [8] K. A. Dick, K. Deppert, L. Samuelson, and W. Seifert. Optimization of au-assisted inas nanowires grown by movpe. *Journal Of Crystal Growth*, 297(2):326–333, 2006. article Compaq_Owner.
- [9] T. Dickinson, J. White, J. Kauer, and D. Walt. Current trends in artificial-nose technology. *TIBTECH*, 16:250, 1998.
- [10] J. Eymery, F. Rieutord, V. Favre-Nicolin, O. Robach, Y. M. Niquet, L. Froberg, T. Martensson, and L. Samuelson. Strain and shape of epitaxial inas/inp nanowire superlattice measured by grazing incidence x-ray techniques. *Nano Letters*, 7(9):2596–2601, 2007. article Compaq_Owner.
- [11] C. Fasth, A. Fuhrer, M. T. Bjork, and L. Samuelson. Tunable double quantum dots in inas nanowires defined by local gate electrodes. *Nano Letters*, 5(7):1487–1490, 2005. article Compaq_Owner.
- [12] A. Görling and M. Levy. Requirements for correlation energy density functionals from coordinate transformations. *Phys. Rev. A*, 45(3):1509–1517, Feb 1992.

-
- [13] F. Herman, J. P. Van Dyke, and I. B. Ortenburger. Improved statistical exchange approximation for inhomogeneous many-electron systems. *Phys. Rev. Lett.*, 22(16):807–811, Apr 1969.
- [14] J. Heyd, J. E. Peralta, G. E. Scuseria, and R. L. Martin. Energy band gaps and lattice parameters evaluated with the heyd-scuseria-ernzerhof screened hybrid functional. *The Journal of Chemical Physics*, 123(17):174101, 2005.
- [15] P. Hohenberg and W. Kohn. Inhomogeneous electron gas. *Phys. Rev.*, 136(3B):B864, 1964.
- [16] D. James, S. Scott, Z. Ali, and W. OHar. Chemical sensors for electronic nose system. *Microchim. Acta*, 149:117, 2005.
- [17] R. O. Jones and O. Gunnarsson. The density functional formalism, its applications and prospects. *Rev. Mod. Phys.*, 61(3):689–746, Jul 1989.
- [18] D. R. Kauffman and A. Star. Carbon nanotube gas and vapor sensors. *Angew. Chem. Int. Ed.*, 4:2–23, 2008.
- [19] C. Kittel. *Introduction to Solid State Physics (6th edition)*. John Wiley and Sons, 1986.
- [20] W. Kohn and L. J. Sham. Self-consistent equations including exchange and correlation effects. *Phys. Rev.*, 140(4A):A1133, 1965.
- [21] H.-P. Komsa, E. Arola, E. Larkins, and T. Rantala. Band offset determination of the gaas/gaasn interface using the density functional theory method. *J. Phys.: Condens. Matter*, 20:315004, 2008.
- [22] J. Lambe and R. C. Jaklevic. Molecular vibration spectra by inelastic electron tunnelling. *Physical Review*, 165:821–832, 1968.
- [23] M. Levy. Density-functional exchange correlation through coordinate scaling in adiabatic connection and correlation hole. *Phys. Rev. A*, 43(9):4637–4646, May 1991.
- [24] M. Levy and J. P. Perdew. Density functionals for exchange and correlation energies: Exact conditions and comparison of approximations. *Int. J. Quantum Chem.*, 49(4):539–548, 1994.
- [25] E. H. Lieb and S. Oxford. Improved lower bound on the indirect coulomb energy. *Int. J. Quantum Chem.*, 19(3):427–439, 1981.
- [26] R. M. Martin. *Electronic Structure: Basic Theory and Practical Methods*. Cambridge University Press, 2004.
- [27] J. E. Peralta, J. Heyd, and G. E. Scuseria. Spin-orbital and energy band gaps calculated with hyed-scuseria-ernzerhof screened hybrid functional. *Phys. Rev. B*, 74:073101, 2006.
- [28] J. P. Perdew. Accurate density functional for the energy: Real-space cutoff of the gradient expansion for the exchange hole. *Phys. Rev. Lett.*, 55(16):1665–1668, Oct 1985.
- [29] J. P. Perdew and K. Burke. Comparison shopping for a gradient-corrected density functional. *Int. J. Quantum Chem.*, 57(3):309–319, 1996.
- [30] T. Shimanouchi. *Tables of Molecular Vibrational Frequencies Consolidated Volume I*. National Bureau of Standards, 1972.
- [31] P. J. Stephens, F. J. Devlin, C. F. Chabalowski, and M. J. Frisch. Ab initio calculation of vibrational absorption and circular dichroism spectra using density functional force fields. *J. Phys. Chem.*, 98(45):11623–11627, 1994.
- [32] B. C. Stipe, M. A. Rezaei, and W. Ho. Single-molecule vibrational spectroscopy and microscopy. *Science*, 280:1732–1735, 1998.
-

- [33] A. M. Stoneham. *Theory of Defects in Solids*. Clarendon Press, Oxford, 1975.
- [34] S. Tomić, B. Montanari, and N. M. Harrison. The group iii-v's semiconductor energy gaps predicted using the b3lyp hybrid functional. *Physica E*, 40:2125–2127, 2008.
- [35] L. Turin. A spectroscopic mechanism for primary olfactory reception. *Chemical Senses*, 21:773–791, 1996.
- [36] L. Turin. Rational odorant design. In D. Rowe, editor, *Chemistry and Technology of Flavours and Fragrances*. Blackwells, 2005.
- [37] M. Zervos and N. T. Pelekanos. Current transport in semiconductor nanowires with built-in barriers based on a 1d transfer matrix calculation. *J. Appl. Phys.*, 104:054302, 2008.

6 List of Symbols, Abbreviations and Acronyms

V	Bias
h, \hbar	Planck's constant
e	Electronic charge
ν	Vibrational frequency
D	Donor level
A	Acceptor level
ΔE	Difference in energy between donor and acceptor
I-V	Current versus voltage
InAs, InP	Indium Arsenide, Indium Phosphide
m_e	Mass of electron
m_W^*	Effective mass of electron in InAs (well)
m_B^*	Effective mass of electron in InP (barrier)
Ry	Rydberg (13.6058 eV)
a_0	Bohr radius (0.529177Å)
E, ϵ	Electron energy
eV	Unit of energy (1.60219×10^{-19} J)
ϵ_0	Permittivity of free space
ϵ_r	Relative permittivity
ρ	Electron density
ρ_0	Reference electron density
$v(z)$	One dimensional effective potential
\mathcal{E}	Electric field
μ	Chemical potential
ψ	Wavefunction
R, Φ, Z	Components of the wavefunction
δ	Mesh point separation
γ	Charge decay distance
α	Effective total electron wave vector
q	Longitudinal electron wave vector
k	Radial electron wave vector
m	Angular quantum number
J_m	Bessel function of the first kind
t_N	Transmission amplitude
f	Fermi function
T	Transmission
$n(\mathbf{r})$	Electron density
$\epsilon_n(\mathbf{k})$	Band energies
$V_{Hartree}$	Hartree potential
V_{xc}	Exchange and correlation potential
$g(\epsilon)$	Density of states
IETS	Inelastic Electron Tunneling Spectroscopy
RTD	Resonant Tunneling Diode
TBDW	Triple Barrier Double Well
NDIR	Nondispersive Infrared
DFT	Density Functional Theory
LDA	Local Density Approximation
GGA	Generalized Gradient Approximation